

Determination of characteristic lengths and times for wormlike micelle solutions from rheology using a mesoscopic simulation method

Weizhong Zou and Xueming Tang

*Department of Chemical Engineering, University of Michigan,
Ann Arbor, Michigan 48109*

Mike Weaver

Analytic Sciences, The Procter & Gamble Company, Mason, Ohio 45040

Peter Koenig

*Computational Chemistry, Modeling and Simulation, The Procter & Gamble
Company, West Chester, Ohio 45069*

Ronald G. Larson^{a)}

*Department of Chemical Engineering, University of Michigan,
Ann Arbor, Michigan 48109*

(Received 2 February 2015; final revision received 11 April 2015;
published 7 May 2015)

Abstract

We apply our recently developed mesoscopic simulation method for entangled wormlike micelle (WLM) solutions to extract multiple micellar characteristic lengths and time constants: i.e., average micelle length, breakage rate, and entanglement and persistence lengths, from linear rheological measurements on commercial surfactant solutions, one containing sodium lauryl ether sulfate (SLE1S), and the other containing both SLE1S and cocamidopropyl betaine, as well as a perfume mixture, in both cases with a sample salt (NaCl) added. Measurements include both mechanical rheometry and diffusing wave spectroscopy, the latter providing the high-frequency data needed to determine micelle persistence length accurately. By fitting the experimental data (G' and G'') across the entire frequency range through our iteration procedure, the method is of practical use in predicting micellar parameters, which are difficult to obtain from other theoretical or experimental methods. The dependence of micellar parameters on added salt concentration, and the effect of micelle breakage mechanisms on viscoelasticity of WLM solutions, are also discussed. © 2015 The Society of Rheology.
[\[http://dx.doi.org/10.1122/1.4919403\]](http://dx.doi.org/10.1122/1.4919403)

^{a)} Author to whom correspondence should be addressed. Fax: (734) 763-0459. Electronic mail: rlarson@umich.edu

I. INTRODUCTION

Surfactant solutions containing self-assembled micelles and other structures are widely used in many applications, due to their various equilibrium aggregation states (oblate or prolate spheroids, short rods or long worms, and disks) [Pérez *et al.* (2014)] and physicochemical properties (density, viscoelasticity, conductivity, solubility, and surface tension) [Zdziennicka *et al.* (2012)]. Induced by changes in temperature, pH, type and concentration of surfactant and salt, morphology transitions between different structures have been extensively investigated [Bernheim-Groswasser *et al.* (2000); Baccile *et al.* (2012); Kusano *et al.* (2012); Yusof and Khan (2012)], leading, for example, to creation of micellar solutions whose rheological properties (viscoelasticity) are tunable by light [Ketner *et al.* (2007); Lu *et al.* (2013)], temperature [Kalur *et al.* (2005)], and additives [Sreejith *et al.* (2011); de Silva *et al.* (2013)]. When long wormlike micelles (WLMs) form, via reversible breaking and rejoining, the solution exhibits viscoelastic behavior through intermicellar entanglements or networks [Cates and Candau (1990); Khatory *et al.* (1993a)]. Applications of WLM solutions are found in shampoo and detergent formulations, drag reduction [Shi *et al.* (2014)], rheology modification [Beaumont *et al.* (2013)], colloid stabilization [James and Walz (2014)], and templated synthesis of nanoparticles [Romano and Kurlat (2000)] and molecular sieves [Beck *et al.* (1992)].

Combinations of different experimental methods, including traditional temperature jump (T-jump) experiments [Waton and Zana (2007)], mechanical rheometry [Khatory *et al.* (1993b)], birefringence [Shikata *et al.* (1994)], light and neutron scattering [Imae and Ikeda (1986); Marignan *et al.* (1989); Jensen *et al.* (2013)], turbidity [Razak and Khan (2013)], and more recently diffusing wave spectroscopy (DWS) [Galvan-Miyoshi *et al.* (2008)], neutron spin echo (NSE) [Nettesheim and Wagner (2007)], and nuclear Overhauser effect spectroscopy (NOESY) [Padia *et al.* (2014)], are often needed to achieve a thorough characterization of micellar properties [Croce *et al.* (2003); Kuperkar *et al.* (2008)]. Theories have also been developed to extract information about micellar kinetics and thermodynamics from experimental data [Ilgenfritz *et al.* (2004); Babintsev *et al.* (2014)]. For WLMs, a particularly important theory is that of Cates and coworkers [Turner and Cates (1991)], which allows average micelle length and rate of breakage to be extracted from linear rheology. Although many improvements to the original Cates' theory have been made [Granek and Cates (1992); Granek (1994)], shortcomings still exist, and continued efforts are required to make its predictions more quantitative [Larson (2012); Zou and Larson (2014)].

Our recently developed “pointer” simulation method [Zou and Larson (2014)] is capable, we believe, of estimating micellar parameters more quantitatively than is possible using previous methods based on Cates' theory [Turner and Cates (1991)]. In what follows, after reviewing both Cates' theory and our simulation model in Sec. II, we present a brief description of experimental methods and surfactant solutions used to obtain rheological data in Sec. III. Using improved empirical relationships between micellar parameters and local rheological behaviors, Sec. IV presents a detailed data-fitting procedure that yields properties of WLMs from rheological data, and Sec. V contains the associated sensitivity studies as well as fitting results for several micellar solutions. The effect of different breakage mechanisms and the possibility of branched micelle detection through our simulation method are also discussed in Sec. V. Conclusions are presented in Sec. VI.

II. MODEL REVIEW

A. Cates' theory

Porte *et al.* (1980) suggested that WLMs be regarded as semiflexible chains rather than as rigid rods, after the micelle persistence length was first measured in 1980. Since

then, many similarities in rheology between WLM and polymer solutions have been noted [Candau *et al.* (1989); Cates and Candau (1990)]. However, a major difference between these two kinds of solutions is the “living” feature of micelles: i.e., their incessant and random breaking and rejoining at thermal equilibrium, which yields a Poisson exponential length distribution [Cates (1987)]

$$N(L) \sim \exp(-L/\langle L \rangle), \quad (1)$$

where L is the length of an individual micelle, and $\langle L \rangle$ is the average micelle length.

Using the polymer “tube model” [Doi and Edwards (1986)] and reptation theory [de Gennes (1979)], Cates (1987) explained the unique Maxwellian (i.e., single-exponential) stress relaxation behavior observed for entangled WLM solutions in which diffusion of WLMs is limited to “tube”-like region by entanglements. His theory is based on the interplay of two mechanisms: i.e., breakage/rejoining and reptation. Imposition of a small step strain on entangled WLMs takes their conformations out of equilibrium, producing a stress. In the absence of breakage, micelle segments can only relax the stress by diffusing curvilinearly, or “reptating,” out of the initial tube, which leads to a loss of original, oriented tube segments as the micelle vacates them. The characteristic time for reptation-induced relaxation depends on the curvilinear diffusivity (D_c) of the micelle along the tube, and the length of the tube (L_t , which is proportional to the length of the micelle L). For micelles with an average length $\langle L \rangle$, the reptation time ($\bar{\tau}_{rep}$) is given by

$$\bar{\tau}_{rep} = \frac{\langle L_t \rangle^2}{\pi^2 D_c}, \quad D_c \equiv \frac{k_B T}{\zeta \langle L \rangle}, \quad (2)$$

where k_B and ζ are Boltzmann’s constant and the longitudinal drag coefficient per unit length of the micelle, respectively.

The above relaxation mechanism is well understood for ordinary “dead” polymers [Doi and Edwards (1986); Likhtman and McLeish (2002)], where no breakage or rejoining exists. For living WLMs, micellar breakage accelerates the relaxation by creating new ends. To address this effect, a dimensionless breakage rate (ς) is defined [Cates (1987)]

$$\varsigma \equiv \frac{\bar{\tau}_{br}}{\bar{\tau}_{rep}}, \quad \bar{\tau}_{br} = \frac{1}{k \langle L \rangle}, \quad (3)$$

where $\bar{\tau}_{br}$, called the average breakage time, is the lifetime a micelle of average length survives before breakage, while k is the breakage rate per unit length.

When ς decreases below unity, the relaxation spectrum is narrowed, since for a high breakage rate the distance that a micelle segment must travel to diffuse out of its tube becomes independent of the tube length. For WLM solutions with $\varsigma \ll 1$, the polydispersity in length distribution therefore has little effect on the relaxation: All tube segments are lost at the same rate and the stress relaxes mono-exponentially. In that case, the stress relaxation time (which is approximated as the reciprocal of crossover frequency ω_{cross} of the storage or elastic modulus G' with the loss or viscous modulus G'') is given as [Cates (1987)]

$$\tau \cong 1/\omega_{cross} \sim \bar{\tau}_{rep} \varsigma^{0.5}, \quad \varsigma \ll 1. \quad (4)$$

The ideal single exponential relaxation behavior, alluded to above, is captured by Cates' original theory, and reveals itself in a perfect semicircular Cole-Cole plot (of G'' versus G') [Cates and Candau (1990)]. Deviations from the perfect semicircle are observed experimentally [Turner and Cates (1991)], however, at high frequencies, implying that some relaxation mechanisms are missing from the original theory. Thus, “breathing” fluctuations, also called “contour length fluctuations” (CLFs) and high-frequency Rouse modes [Dealy and Larson (2005)] were subsequently incorporated into the theory [Granek and Cates (1992); Granek (1994)]. Using the modified theory, the average micelle length $\langle L \rangle$ can be estimated from the observed minimum in G'' (G''_{min}) at high frequency by [Granek (1994)]

$$\frac{G''_{min}}{G_N} = \left(\frac{l_e}{\langle L \rangle} \right)^{0.8} = \bar{Z}^{-0.8}, \quad (5)$$

where l_e is the micelle entanglement length, and \bar{Z} is the number of entanglements for micelles with average length $\langle L \rangle$. G_N is the plateau modulus, which can be calculated theoretically from [Cates (1988)]

$$G_N \cong \frac{k_B T}{l_e^{1.8} l_p^{1.2}}, \quad (6)$$

where l_p is the micelle persistence length.

By assuming WLMs have a persistence length of 15 nm, a method [Turner and Cates (1991)] was developed to determine the average micelle length ($\langle L \rangle$) and dimensionless breakage rate (ς) indirectly from rheological data, since these quantities are essentially impossible to obtain directly from other experiments. However, as we discussed in our earlier work [Zou and Larson (2014)], the accuracy of the method is limited by the assumptions of both the theory and the approximations used to extract micelle parameters from individual features of the rheological curves (G' and G''), and by possible inaccuracy in the assumed value of the persistence length. Hence, it is desirable to overcome these limitations, by developing a more advanced predictive model, discussed next.

B. Simulation model

We extended Cates' theory by developing a simulation-based mesoscopic model [Zou and Larson (2014)] for entangled WLM solutions, allowing more quantitative estimates of multiple characteristic micellar parameters. The new model includes important physics neglected in the earlier Cates' theories [Cates (1987); Cates (1988); Turner and Cates (1991); Granek and Cates (1992); Granek (1994)], i.e., tube rearrangement, micelle semiflexibility, and high-frequency bending modes. Derived from the expression for CLF-induced relaxation of linear polymers [Milner and McLeish (1997, 1998)], the rate of loss of tube segments at the ends of tubes is represented in a time-implicit form in our model to facilitate the addition of contributions from reptation [Zou and Larson (2014)]. The effect of tube rearrangement (i.e., disentanglement-induced relaxation due to the motion of neighboring micelles) is accounted for using “double reptation” [Tuminello (1986); des Cloizeaux (1988)]. Unlike classical polymers, which are flexible enough to coil up within their tubes, WLMs are relatively rigid: They only bend slightly in thin tubes due to a large persistence length (10–150 nm). The semiflexibility of WLMs is characterized by the ratio of micelle entanglement length (l_e) to persistence length (l_p) as

$$\alpha_e \equiv \frac{l_e}{l_p}. \quad (7)$$

If $\alpha_e > 2$, micelles coil up in the tube, which implies that the micelle length is larger than its tube length [Eq. (8a)]. Otherwise, the micelle length is approximately equal to its tube length [Eq. (8b)]

$$L \approx L_t \cdot \sqrt{0.5\alpha_e}, \quad \alpha_e > 2, \quad (8a)$$

$$L \approx L_t, \quad \alpha_e \leq 2. \quad (8b)$$

The former is called the loosely entangled regime, while the latter one, with $\alpha_e < 1$, is the tightly entangled regime. A crossover between these regimes occurs in the range $1 \leq \alpha_e \leq 2$. Detailed information about these regimes can be found in the works of Morse (1998a,b). A formula to calculate the plateau modulus (G_N) for any α_e is [Zou and Larson (2014)]

$$G_N = f(\alpha_e) \cdot 9.75 \frac{k_B T}{\alpha_e^{9/5} l_p^3} + [1 - f(\alpha_e)] \cdot \frac{28}{5\pi} \frac{\phi k_B T}{d^2 \alpha_e l_p}, \quad (9a)$$

where ϕ is the volume fraction of surfactant, and d is the micelle diameter. To get a smooth crossover from loosely (first term) to tightly (second term) entangled regimes, the weighting function $f(\alpha_e)$ is taken to be [Zou and Larson (2014)]

$$f(\alpha_e) = \frac{\alpha_e^3}{3 + \alpha_e^3}. \quad (9b)$$

Note that while this functional form is arbitrary, in the middle of the cross-over, the predictions for G_N from each of the two regimes differ by a factor of less than two, and the cross-over formula [Eq. (9a)] gives a value roughly halfway between the two limits. Hence, the exact functional form is unlikely to matter much.

Bending motions, where micelle segments behave as bendable elastic rods, dominate on length scales smaller than the persistence length, as is revealed in rheological experiments by a three-quarters power law of modulus versus frequency at high frequencies [see Eq. (10a)] [Galvan-Miyoshi *et al.* (2008); Oelschlaeger *et al.* (2009)]. Like the high-frequency Rouse modes [Wang *et al.* (2010)], bending motions [Gittes and MacKintosh (1998)] are incorporated analytically by the following additive contributions to G' and G'' [Zou and Larson (2014)]:

$$G'(\omega) = \text{Re}[i^{3/4}] \frac{\rho}{15} \frac{k_B T}{l_p} (2\omega\tau_p)^{3/4}, \quad G''(\omega) = \text{Im}[i^{3/4}] \frac{\rho}{15} \frac{k_B T}{l_p} (2\omega\tau_p)^{3/4} + \omega\eta_s, \quad (10a)$$

$$\text{with } \rho = \frac{4\phi}{\pi d^2}, \quad \tau_p = \frac{\zeta_{\perp} l_p^3}{k_B T}. \quad (10b)$$

In the above, “ $\text{Re}[\cdot]$ ” and “ $\text{Im}[\cdot]$ ” refer to real and imaginary parts, “ i ” is the imaginary unit, and ρ is the micelle contour length per unit volume, which is related to the micelle diameter (d) and surfactant volume fraction (ϕ) by Eq. (10b). Note that Eq. (10b) involves a constant ζ_{\perp} describing the drag coefficient for perpendicular bending motions

[Morse (1998b)], which should be distinguished from the longitudinal drag coefficient ζ for reptation in Eq. (2), i.e.,

$$\zeta = \frac{2\pi\eta_s}{\ln(\alpha_e^{0.6}l_p/d)}, \quad \zeta_{\perp} = \frac{4\pi\eta_s}{\ln(0.6\alpha_e^{0.6}l_p/d)}, \quad (11)$$

where η_s is the solvent viscosity.

Apart from relaxation mechanisms, innovations in modeling breakage/rejoining and converting data from time to frequency enable fast simulations with an ensemble of 5000 WLMs by our mesoscopic method. Using pointers to track the locations of the ends of unrelaxed tube segments along discretized micellar chains, the number of pointers and their relative positions vary with time: Pointers can be created by breakage and moved and finally annihilated by chain relaxation through reptation and CLFs. By summing the fraction of unrelaxed tube segments, the time-dependent stress relaxation function $[\mu(t)]$ can be calculated and squared to incorporate constraint release using the double reptation ansatz. Although largely empirical, we use double reptation since it has proven to be accurate for polydisperse polymers, and because no general, rigorous theory has been developed for constraint release in micelles with incessant breakage and rejoining. A schematic of the above procedure (called the “pointer algorithm”) is shown in Fig. 1, details of which can be found in our previous paper [Zou and Larson (2014)].

Due to the failure of traditional Fourier transform methods as micellar parameters vary, a modified genetic algorithm (GA) is applied to facilitate the transformation of $\mu^2(t)$ to the frequency domain with high-frequency relaxation mechanisms added through an analytical function G^H [Zou and Larson (2014)]. Hence, our simulation model can be expressed in the following functional form:

$$G^*(\omega) = G_N \mathcal{F}[\mu^2(t, \varsigma, \langle L \rangle, \alpha_e, d)] + G^H(\omega, G_N, \langle L \rangle, \alpha_e, d), \quad (12)$$

where $G^*(\omega)$ is the complex modulus, whose real and imaginary parts are $G'(\omega)$ and $G''(\omega)$, respectively. The operator $\mathcal{F}[\cdot]$ denotes the time-to-frequency transformation through a modified GA. On the right side of the above equation, the first term accounts for contributions from low frequency relaxation mechanisms: Reptation, CLFs, and tube rearrangement; while the second term represents analytical expressions for high-frequency Rouse and bending motions.

According to Eq. (12), five characteristic parameters are used to predict the rheological behavior of WLM solutions, i.e., plateau modulus (G_N), dimensionless breakage rate

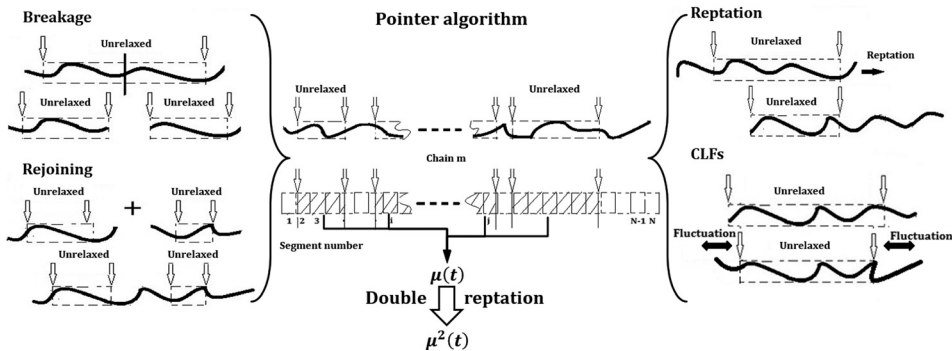


FIG. 1. Schematic of pointer algorithm, showing the creation and movement of pointers by breakage and rejoining (left), and reptation and CLFs (right). In the center panel, the hatched zones represent unrelaxed tube segments.

(ζ), average micelle length ($\langle L \rangle$), semiflexibility coefficient (α_e), and micelle diameter (d). Temperature (T), surfactant volume fraction (ϕ), and solvent viscosity (η_s) are known experimental parameters and not counted here as model parameters. Thus, by fitting rheological data with our simulation model, estimates for the five micellar parameters (G_N , ζ , $\langle L \rangle$, α_e , d) can be obtained.

III. EXPERIMENTAL SECTION

The WLM solutions used in this paper are aqueous solutions of SLE1S [sodium lauryl one ether sulfate, Fig. 2(a)] and a mixture of SLE1S and CAPB [cocamidopropyl betaine, Fig. 2(b)] at 25 °C. A simple salt (sodium chloride, NaCl) is added to both solutions, while the latter one also contains a 1 wt. % perfume mixture. Due to the complexity of these commercial materials, a weight percentage instead of molar concentration is used here. An 11 wt. % SLE1S/CAPB solution contains 9.85 wt. % SLE1S and 1.15 wt. % CAPB, where SLE1S is an abbreviation for commercial sodium lauryl ether sulfate with one ethoxyl group on average (but with polydispersity about this average); and CAPB is the co-surfactant. The perfume mixture consists of six organic components with their corresponding weight percentages, i.e., (i) synambrian (CAS number: 6790-58-5, 10.7 wt. %); (ii) linalool (CAS number: 78-70-6, 23.3 wt. %); (iii) allylamylglycolate (CAS number: 67634-00-8, 13.5 wt. %); (iv) beta-ionone (CAS number: 14901-07-6, 11.5 wt. %); (v) heliotropin (CAS number: 120-57-0, 15.4 wt. %); and (vi) undecavertol (CAS number: 81782-77-6, 25.6 wt. %). The rheological properties of samples were measured by a TA Instruments DHR3 controlled-stress rheometer with TRIOS software using a 60 mm aluminum, 2°-cone. The cone geometry was inertially corrected prior to measurement, and the air bearing mapped in precision mode as prescribed in the TRIOS software. The frequency spectrum was collected using either 1% or 10% strain amplitude from 0.1 to 500 rad/s, but edited to include only data where the raw phase angle was below the 180° limit in TRIOS software. For these samples, this usually limited the frequency spectrum to 250–316 rad/s, and abrupt changes in moduli (most easily indicated in $\tan \delta$) would be rejected. For the former solution, DWS is also applied to get the high-frequency behavior (1–150 000 rad/s). The wavelength of light and the diameter of beads used in DWS are 532 and 630 nm, respectively. The beads are made of IDC polystyrene latex from Life Technologies (cat# S37495) with hydrophobic surface, which are stabilized with a low level of sulfate charges and surfactant free. The WLM solution samples for DWS measurement were mixed with 0.5 wt. % beads before adding salt to ensure good mixing prior to thickening with salt. After 12 h equilibration, samples were measured in 5 mm glass cells on LS Instruments RheoLab II system. The transport mean free path l^* ($= 580 \mu\text{m}$) was determined from the control sample with the same-size beads in water. Details about DWS can be found in the works of [Buchanan *et al.* \(2005\)](#), [Galvan-Miyoshi *et al.* \(2008\)](#), and [Oelschlaeger *et al.* \(2009\)](#). Samples were both prepared and measured at the Procter & Gamble company.

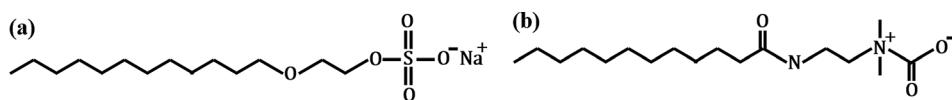


FIG. 2. Molecular structure of (a) SLE1S and (b) CAPB.

IV. DATA-FITTING PROCEDURE

A. Empirical correlations

As shown in our previous paper [Zou and Larson (2014)], empirical relationships between local rheological features and micellar parameters are constructed from simulation results using the pointer algorithm to obtain good initial guesses of WLM properties. These features are the local maximum and minimum values of G'' along with the corresponding frequencies, denoted as $(\omega_{max}, G''_{max})$ and $(\omega_{min}, G''_{min})$, respectively. Motivated by the work Cates and coworkers [Turner and Cates (1991); Granek (1994)], G''_{max}/G_N , or the height of the semicircle on the normalized Cole-Cole plot, is related to the dimensionless breakage rate (ς), while the “dip” at high frequencies (i.e., G''_{min}/G_N) is related to the dimensionless average tube length $[\bar{Z}_t$, defined in Eq. (13b)]. Instead of using the stress relaxation time $[\tau$, Eq. (4)], ω_{max} is introduced to extract the characteristic time (i.e., reptation time, $\bar{\tau}_{rep}$) from the frequency information. An illustration for these local features is shown in Fig. 3, along with empirical correlations for the above quantities, given in our previous paper [Zou and Larson (2014)], and repeated here as Eq. (13), given below

$$\omega_{max} \bar{\tau}_{rep} = B \cdot \varsigma^{-0.63}, \quad B = 2.1, \quad 1 < \alpha_e < 3, \quad (13a)$$

$$\frac{G''_{min}}{G_N} = C \bar{Z}_t^{-0.61}, \quad \bar{Z}_t = \frac{\langle L_t \rangle}{l_e}, \quad 1 < \alpha_e < 3, \quad (13b)$$

$$\frac{G''_{max}}{G_N} = -0.0657 \log(\varsigma) + 0.265, \quad \bar{Z} = \frac{\langle L \rangle}{l_e} > 10. \quad (13c)$$

Since the above correlations are only accurate over a limited range of α_e and \bar{Z} (average entanglement number), their corresponding extensions are achieved by replacing the pre-factor B with a function of α_e for Eq. (13a) and \bar{Z}_t with \bar{Z} for Eq. (13b) in what follows. Note that “log” and “ln” denote the logarithmic base of 10 and e , respectively.

By fixing ς ($= 0.05$), a log-log plot of $\omega_{max} \bar{\tau}_{rep}$ versus α_e is obtained in Fig. 4(a), with a power-law exponent of 3. From Fig. 4(b), the dependence of $\omega_{max} \bar{\tau}_{rep} \alpha_e^{-3}$ on ς and the

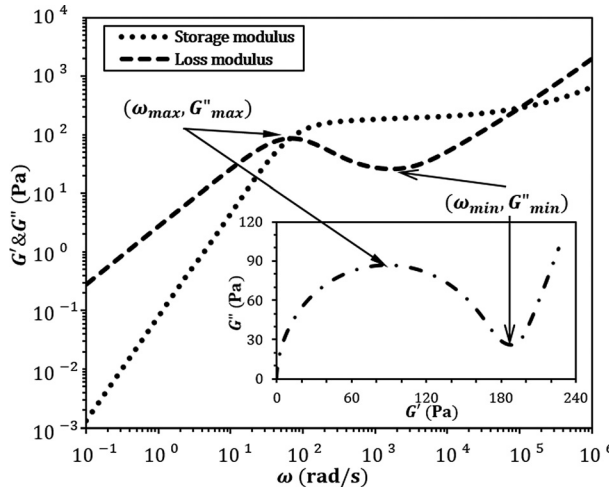


FIG. 3. Illustration of local rheological features. Inset: Cole-Cole plot.

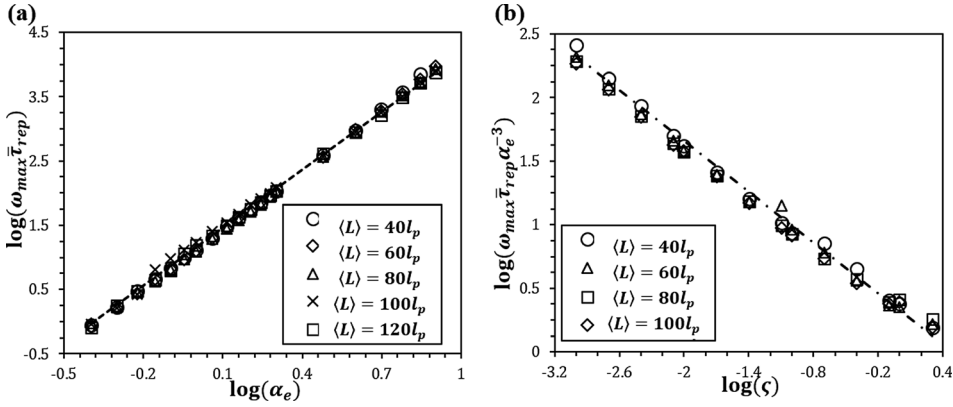


FIG. 4. Extended empirical correlation for the dependence of $\omega_{\max} \bar{\tau}_{\text{rep}}$ on semiflexibility coefficient $\alpha_e = l_e/l_p$ and dimensionless breakage rate ζ with $l_p = 25$ nm and $d = 5$ nm. (a) The linear fit (dashed line) on the log-log plot has a slope of 3 with $R^2 = 0.999$ for fixed $\zeta = 0.05$. (b) The linear fit (dashed-dotted line) on the log-log plot has a slope of $-2/3$ and intercept of $\log 2$ when $\log(\zeta) = 0$ with $R^2 = 0.995$. Note that data in the above figures all come from simulations.

associated prefactor are obtained by the slope and intercept with $\log(\zeta) = 0$, respectively, according to the linear fit on the log-log plot. The extended formula, covering the experimentally relevant range of α_e (0.3–8) is given in Eq. (14a).

By plotting G''_{\min}/G_N against \bar{Z} logarithmically in Fig. 5, the exponent of the power-law correlation between these two quantities is obtained in each of three regions whose range depends on the specific value of ζ . When \bar{Z} is small, WLMs are short and loosely entangled, and the exponent is -1 (denoted by the slope of solid lines in Fig. 5). Once \bar{Z} becomes larger than a critical value (\bar{Z}_c), the exponent changes to $-3/4$, shown by the slope of dashed lines in Fig. 5, which is close to the power-law prediction of Cates and coworkers [-0.8 , Eq. (5)]. Micelle semiflexibility (α_e) has no effect on this power-law dependence: The data points for micelles with different $\langle L \rangle$ and α_e merge onto common curves (denoted by dashed lines in Fig. 5). However, if WLMs are entangled tightly enough ($\alpha_e < 1.5$), deviations from the above common curves appear as dashed-dotted parallel lines with a slope of $-1/5$ in Fig. 5. Note that the range of the first region ($\bar{Z} < \bar{Z}_c$) varies with ζ : An increase of ζ decreases \bar{Z}_c , thus limiting its range. The relationship between \bar{Z}_c and ζ is given in Eq. (14b).

The above-extended empirical correlations are summed up as

$$\omega_{\max} \bar{\tau}_{\text{rep}} = 2\alpha_e^3 \zeta^{-2/3}, \quad (14a)$$

$$\frac{G''_{\min}}{G_N} = C \bar{Z}^{-a} \text{ with } \bar{Z}_c = \zeta^{-3/4} \begin{cases} a = 1, & C \cong \zeta^{-1/4}, & (\bar{Z} \leq \bar{Z}_c \text{ and } \alpha_e > 1.5), \\ a = \frac{3}{4}, & C \cong \zeta^{-1/16}, & (\bar{Z} > \bar{Z}_c \text{ and } \alpha_e > 1.5), \\ a = \frac{1}{5}, & C \cong \zeta^{-1/16} \left(\frac{2\langle L \rangle}{3l_p} \right)^{-11/20}, & (\alpha_e \leq 1.5), \end{cases} \quad (14b)$$

$$\frac{G''_{\max}}{G_N} = -0.0657 \log(\zeta) + 0.265. \quad (14c)$$

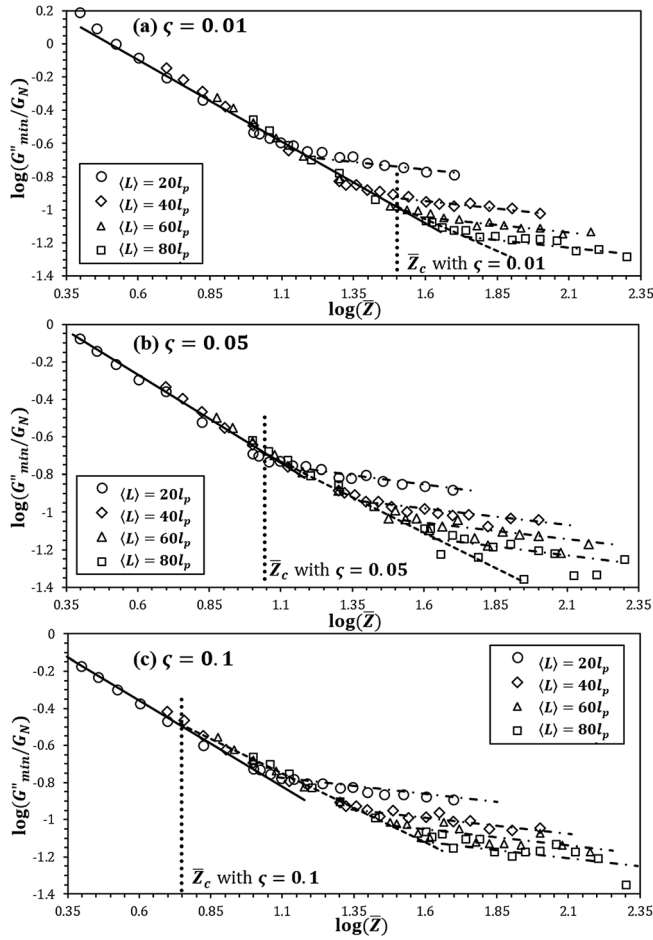


FIG. 5. Extended empirical correlation for the dependence of G''_{\min}/G_N on average entanglement number (\bar{Z}) by varying average micelle length ($\langle L \rangle$) and semiflexibility coefficient (α_e) with $l_p = 25$ nm and $d = 5$ nm. (a) $\zeta = 0.01$; (b) $\zeta = 0.05$; and (c) $\zeta = 0.1$. Note in the above figures that the slope of solid lines, dashed lines, and dotted-dashed lines are -1 , $-3/4$, and $-1/5$, respectively, and all the data are from simulations.

Note that the above correlations [Eq. (14)] are all based on simulation results with $10^{-3} < \zeta < 10$, $0.3 < \alpha_e < 8$ (these ranges encompass the values typical of actual WLM solutions), and well-defined local maximum and minimum G''_{\max} and G''_{\min} , but are nearly independent of micelle persistence length l_p and diameter d which have only a small effect on data normalized by G_N at frequencies below that at which G'' has its minimum, G''_{\min} [Zou and Larson (2014)]. If there is no well-defined maximum and minimum in G'' , the crossover frequency (ω_{cross}) and the corresponding $G''(\omega_{\text{cross}})$ will be treated as ω_{\max} and $G''_{\max}(=G''_{\min})$, respectively. This situation usually occurs for WLM solutions with $\bar{Z} \ll \bar{Z}_c$. (Where there is a maximum in G'' , the difference between G''_{\max} and the crossover point $G''(\omega_{\text{cross}})$ is only about a few percent of the plateau modulus (G_N), and we therefore do not expect there to be a large difference in results obtained using the cross-over point, instead of the maximum in G'' .)

The empirical correlations in Eq. (14) are useful for inferring the properties of WLM solutions from rheological data (G' and G''). As an example, we consider the temperature-dependent rheological data in Fig. 6 from Siriawatwechakul *et al.* (2004),

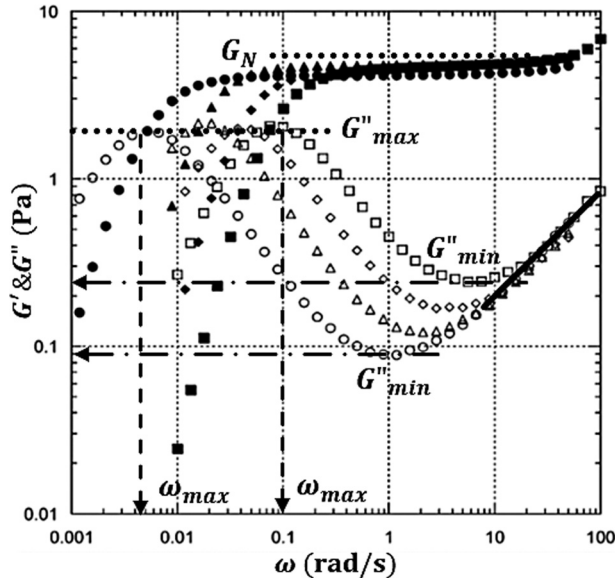


FIG. 6. Temperature-dependent rheological data from [Siriwatwechakul et al. \(2004\)](#), showing temperature shifts of G''_{max} , G''_{min} , and ω_{max} . Circles: $T = 25^\circ\text{C}$; triangles: $T = 35^\circ\text{C}$; diamonds: $T = 40^\circ\text{C}$; and squares: $T = 45^\circ\text{C}$.

which is for a 2 wt. % erucyl bis (hydroxyethyl) methylammonium chloride (EHAC) surfactant solution with added 4 wt. % potassium chloride (KCl) salt. From the lowest temperature (25°C , denoted by circles) to the highest one (45°C , denoted by squares), the value of G''_{min} triples while G''_{max} and G_N (plateau modulus, denoted by the magnitude of the plateau region for G') remain constant. A frequency shift is also observed with around a 30-fold increase of ω_{max} .

Since $G''_{max} (\cong 2 \text{ Pa})$ and $G_N (\cong 5 \text{ Pa})$ remain unchanged, according to Eq. (14c), ζ can be taken as a constant, which is approximately equal to 0.01. Assuming the solution lies in the loosely entangled regime ($\alpha_e > 2$), then $\bar{Z} < 0.5\langle L \rangle/l_p$, and if $\zeta = 0.01$, as shown by the solid line in Fig. 5(a), the power-law dependence of G''_{min}/G_N on \bar{Z} [Eq. (14b)] is in the regime where the exponent is -1 , which means

$$\bar{Z} \sim 1/G''_{min}.$$

Based on Eqs. (2), (7), (8a), and the definition of \bar{Z} given in Eq. (13c), we can also find

$$\bar{\tau}_{rep} \sim \langle L \rangle \langle L_t \rangle^2 \sim \bar{Z}^3 l_p^3 \alpha_e^2.$$

For a constant G_N , according to Eq. (9), for the loosely entangled regime [$f(\alpha_e) \approx 1$]

$$\alpha_e \sim l_p^{-5/3}.$$

Then, substituting the above relationships for \bar{Z} , $\bar{\tau}_{rep}$, α_e into Eq. (14a) yields

$$\omega_{max}/G''_{min}^3 \sim l_p^{-14/3}.$$

With an approximate 30-fold and three-fold increase in ω_{max} and G''_{min} , respectively, the above qualitative correlation implies that there is little change in micelle persistence length (l_p) from 25 °C to 45 °C. Thus, in this case temperature has little effect on l_p , which is confirmed by the collapse of the data for G'' at high frequencies (shown by the solid line in Fig. 6, which is a region influenced by persistence length, and would therefore show a shift with temperature if l_p were temperature dependent.)

B. Data-fitting procedure

For quantitative analyses of WLM properties, we develop an iterative experimental data-fitting procedure to achieve accurate estimates of micellar parameters with low fitting errors. The procedure relies heavily on empirical correlations [Eq. (14)] as well as theoretical equations [Eqs. (2), (8), and (9)]. Fitting deviations are calculated separately within each of the four frequency domains depicted in Fig. 7 (low frequency, transition 1, transition 2, and high frequency)

$$\varepsilon_i = \frac{1}{2N_i} \sum_{j=1}^{N_i} \left\{ \ln \left[\frac{G^{fit}_{ij}(\omega_{ij}^{exp})}{G^{exp}_{ij}(\omega_{ij}^{exp})} \right] + \ln \left[\frac{G''^{fit}_{ij}(\omega_{ij}^{exp})}{G''^{exp}_{ij}(\omega_{ij}^{exp})} \right] \right\}, \quad i = 1, \dots, 4, \quad (15a)$$

$$\text{with } \omega_{1,N_1}^{exp} = \omega_{max}^{exp}, \quad \omega_{2,N_2}^{exp} = \omega_{min}^{exp}, \quad \omega_{3,N_3}^{exp} = 10\omega_{min}^{exp}, \quad (15b)$$

where superscripts *exp* and *fit* represent data points from experiment and simulation, respectively. N_i is the number of data points in each frequency range. Note that the above error is not a least-squares error, but is a net deviation in the logarithmic ratio of fitted to experimental results, averaged over each frequency domain. We use this measure of error, because it allows us to use the net deviation direction (positive or negative) in that domain to better determine how to adjust fitting parameters (see Appendix A for details) that are most important for that domain and hence quickly reach an optimal fit (i.e., within around 12 iterations). Such a rapidly converging method is needed because each iteration requires a separate simulation of the relaxation of 5000 micelles and takes 2–3 h on a single CPU. However, the method does require a separate measure of error averaged over each of four separate domains to prevent positive deviations in one domain from

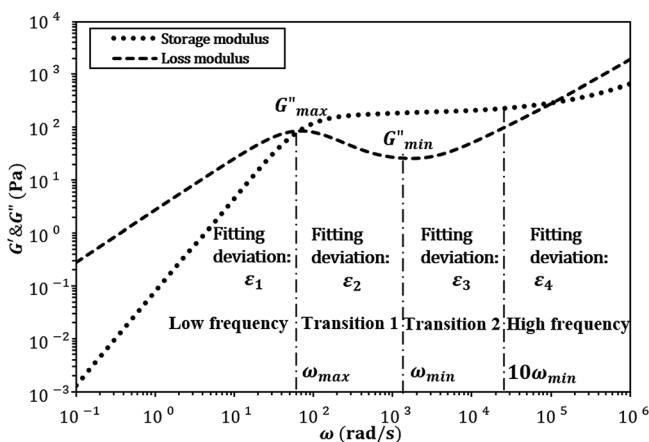


FIG. 7. Definition of frequency regions and associated fitting deviations.

cancelling negative ones in another. The key to the success of this method is the monotonic behavior of G'' within each domain and the dominant effect of just one or two fitting parameters in each domain.

Besides the overall goodness of fit represented by the values of ε_i in Eq. (15), differences between experimental and predicted local features, i.e., the values of $(\omega_{\max}, G''_{\max})$ and $(\omega_{\min}, G''_{\min})$, can also help iterate to a better estimation of parameters, as alluded to above. Although they are not included in the set of five model fitting parameters ($G_N, \zeta, \langle L \rangle, \alpha_e, d$) listed in Eq. (12), other micellar parameters $\bar{\tau}_{rep}$, \bar{Z} [defined in Eqs. (2) and (13c)] as well as $\langle L_t \rangle$, l_e , l_p , ζ [Eqs. (7), (8), and (11)] need to be determined during parameter modification. A “map” (Fig. 8) is established for that purpose, which shows how all the additional parameters ($\bar{\tau}_{rep}$, \bar{Z} , $\langle L_t \rangle$, l_e , l_p , ζ) can be derived from the five independent model parameters ($G_N, \zeta, \langle L \rangle, \alpha_e, d$) along with theoretical relationships [Eqs. (2), (3), (7)–(9), and (11)] and known experimental parameters (T, ϕ, η_s).

The flowchart of the data-fitting procedure is laid out in Appendix A (Fig. 18). At the end of each simulation {details of which can be found in our previous paper [Zou and Larson (2014)]}, fitting deviations ($\varepsilon_1, \varepsilon_2, \varepsilon_3, \varepsilon_4$) are calculated through Eq. (15) and predicted local feature-related points are obtained. Using the parameter map (see Fig. 8), the five independent model parameters ($G_N, \zeta, \langle L \rangle, \alpha_e, d$) from the last round of simulation are converted into $(G_N, \zeta, \bar{\tau}_{rep}, \bar{Z}, l_p)$ for further modifications: Two different routes are taken in alternating steps to minimize both the overall fitting deviations and the difference in local features between experimental points $(\omega_{\max}^{exp}, G''_{\max}^{exp}, \omega_{\min}^{exp}, G''_{\min}^{exp})$ and simulated ones $(\omega_{\max}^{fit}, G''_{\max}^{fit}, \omega_{\min}^{fit}, G''_{\min}^{fit})$, respectively. Detailed equations used to determine the values of five model parameters for the next round of simulation are also derived in Appendix A. The fitting deviations and differences in local features are also used to constrain the modified values of $\zeta, \bar{\tau}_{rep}, l_p$ within ranges of limited width [Eq. (A8), Fig. 19 in Appendix A5], leading to more stable convergence. The code and an example input file can be found under our website: <http://cheresearch.engin.umich.edu/larson/software.html>.

After ~ 6 –8 iterations, the simulated curves typically have average fitting deviations [Eq. (15)] around 10% for each frequency range. In general, 12 iterations are used to achieve the best fit with less than 10% average fitting deviations and the least difference of local-feature points. The computational time is around 6–12 h for a single processor. Since the above procedure is based on the empirical correlations in Eq. (14), in case a well-defined local maximum and minimum are missing, the following substitutions are

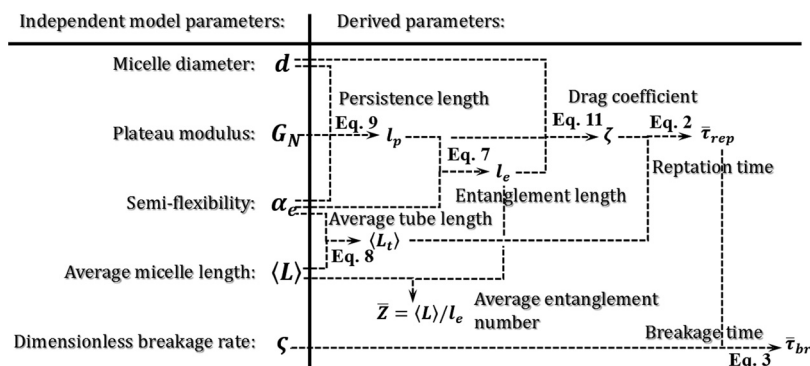


FIG. 8. Parameter map showing relationships between the five independent model parameters ($G_N, \zeta, \langle L \rangle, \alpha_e, d$) and the additional parameters ($\bar{\tau}_{rep}$, \bar{Z} , $\langle L_t \rangle$, l_e , l_p , ζ) derived from them. Arrows point toward quantities derived from the equations given. Dashed lines connect to the input parameters required by the given equation.

made: ω_{\max} ($=\omega_{\text{cross}}$), G''_{\max} ($=G''_{\text{cross}}$), ω_{\min} ($=2\omega_{\max}$), and G''_{\min} ($=G''_{\max}$). As explained in our previous work [Zou and Larson (2014)], our method is incapable of determining micelle diameter (d) from fitting rheological data, but a reasonably accurate value for d can be supplied from other measurements, for instance, small angle neutron scattering (SANS) [Marignan *et al.* (1989)], or from molecular modeling.

V. RESULTS AND DISCUSSION

A. Fitting results

Experimental data and the corresponding fits to mechanical rheometric data, DWS data, and a combination of these two data sets, i.e., mechanical data at low frequencies (<50 rad/s) and DWS data at high frequencies (>50 rad/s), for the same WLM solution (6.67 wt. % SLE1S, 3.10 wt. % NaCl with solvent viscosity $\eta_s = 0.9$ cP at 25 °C) are given in Fig. 9 with resulting estimates of parameters shown in Table I. The persistence length (l_p) over 100 nm is obtained for these micelles formed by SLE1S, which is much greater than that for the classical CTAB or CPyCl [Chen *et al.* (2006)]. The reason for this greater value of l_p , we believe, is due to the larger micelle diameter resulting from the larger headgroup and the longer average tail length of SLE1S surfactant molecule, since the estimation of l_p strongly depends on micelle diameter (see Table IV in Appendix B). We note that in classic beam theory, a solid cylinder has a bending modulus that scales as the fourth power of its diameter, and so a modest 20% increase in diameter can double the persistence length. While micelles are not solid cylinders, by analogy, a steep dependence of persistence length on micelle diameter might nevertheless be expected.

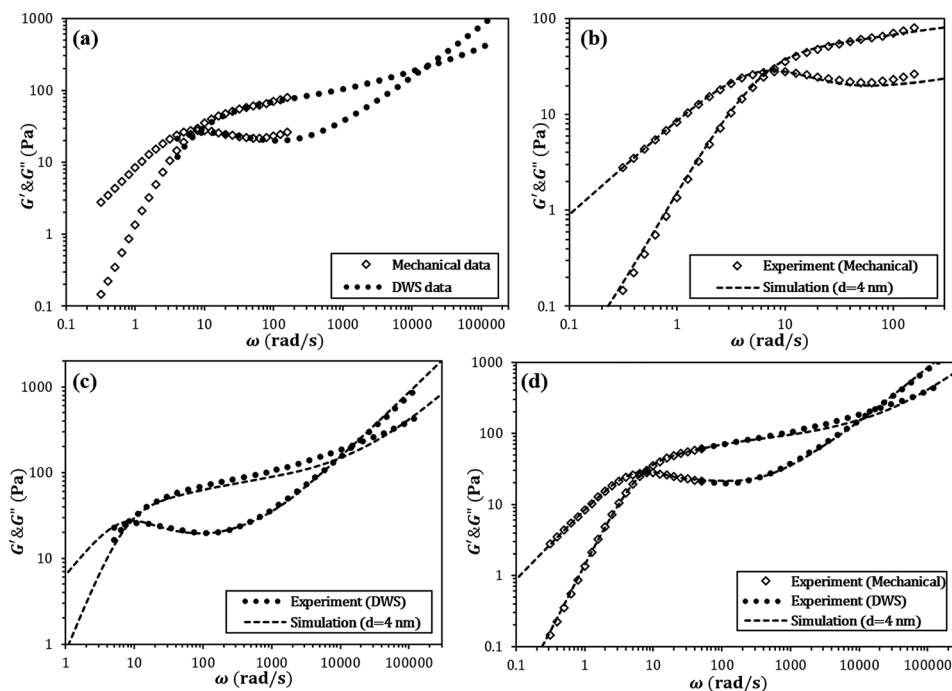


FIG. 9. Experimental data and fitting results with $d = 4$ nm for WLM solution (6.67 wt. % SLE1S, 3.10 wt. % NaCl with solvent viscosity $\eta_s = 0.9$ cP at 25 °C). (a) Experimental data; (b) fits for mechanical rheometric data; (c) fits for DWS data; and (d) fits for combined data.

TABLE I. Estimation of parameters from fits in Figs. 9(b)–9(d).

Parameters	Mechanical data	DWS data	Combined data
G_N (Pa)	115	105	115
ζ	2.49	1.16	1.82
$\langle L \rangle$ (μm)	1.45	1.60	1.59
α_e	1.35	1.41	1.36
d (nm) ^a	4	4	4
l_e (nm)	155	161	153
l_p (nm)	116	114	112

^aThe value of $d = 4$ nm used in simulations for the WLM solution is taken from SANS measurement by our collaborators Karsten Vogtt and Gregory Beaucage at the University of Cincinnati.

According to Fig. 9(a), mechanical rheometric data overlap well with that for DWS in the frequency range from 10 to 50 rad/s. Mismatches at low and high frequencies are attributed to errors in DWS and mechanical rheometry, respectively, which lead to differences in parameter estimates as shown in Table I. For the parameters G_N , ζ , and α_e , the values extracted from DWS data alone deviate more from the values obtained from the combined data than do the values from the mechanical data alone. This suggests a greater importance of low frequency behavior than of high-frequency behavior on estimations of these parameters. The over six frequency-decade fit to the combined data [Fig. 9(d)] with less than 5% absolute average deviation between predicted and measured data points suggests that the viscoelastic behaviors of micelle solutions are well depicted by our simulation method. Although little difference is observed for estimates of all parameters obtained from mechanical and combined data sets (even the persistence length is hardly changed when the DWS data are included as shown by Table I), the accuracies of estimations (i.e., insensitivity percentage discussed later) vary with parameters and availability of high-frequency data (i.e., the data beyond ω_{min}). Thus, while fits using the mechanical data only were adequate for the data of Fig. 9, in general, high-frequency data are important to extract an accurate value of l_p , as is demonstrated in the following sensitivity study.

B. Sensitivity study

Here, the sensitivity of parameter determination to error or noise is assessed by a constrained fitting procedure. For this purpose, the combined (mechanical and DWS) experimental data [Fig. 9(d)] are used with its best-fit parameters shown in Table I. Starting from these best-fit values, we take each parameter, one at a time, and artificially change its value to a new one that deviates from its best-fit value by a given percentage. Then, holding this one parameter value fixed, we adjust the other parameters to obtain constrained best fits to the rheological data. An exception is the value of d , which we hold at 4 nm according to SANS measurements, since its value cannot be accurately determined from rheology as discussed earlier. This inability of rheology to determine micelle diameter is illustrated by Fig. 20 in Appendix B with the corresponding fitted parameters given in Table IV, where no significant difference is observed among fitting curves for micelle diameter varying between 3 and 4.5 nm. (The range encompasses the values typical of actual WLM solutions.) Based on this constrained fitting, the deviation between experimental and fitted curves is a measure of the sensitivity of the fit to the value of the constrained parameter. As an illustration, the effect of varying micelle persistence length (l_p) is given below.

TABLE II. Sensitivity analysis, showing effect of variation in l_p on best-fit values of other parameters for data of Fig. 9(d).

Parameters	70% l_p	80% l_p	90% l_p	Best-fit l_p	110% l_p	120% l_p	130% l_p	140% l_p	150% l_p
G_N (Pa)	138.5	121	114	115	108	104	97.5	95	92
ς	15.58	2.06	1.10	1.82	1.53	0.96	0.76	0.93	0.69
$\langle L \rangle$ (μm)	0.927	1.59	1.80	1.59	1.58	1.83	1.92	1.73	1.87
α_e	1.516	1.497	1.446	1.363	1.341	1.304	1.288	1.261	1.238
l_e (nm)	119	134	146	153	165	176	188	198	208
l_p (nm)	78.5	89.5	101	112	123	135	146	157	168
ε_{max} (%) ^a	20.8	16.2	9.6	4.1	5.3	5.6	10.7	14.8	19.5

^aNote that the error (ε_{max}) is the absolute maximum from the four average fitting derivations [$\varepsilon_1, \varepsilon_2, \varepsilon_3, \varepsilon_4$, defined in Eq. (15)]. By varying l_p from its unconstrained best-fit value, the maximum average fitting deviation occurs in the high-frequency region, as shown by Fig. 10.

As shown by Table II and Fig. 10, a variation of l_p from its best-fit value drives all the other parameters ($G_N, \varsigma, \langle L \rangle, \alpha_e, l_e$) away from their unconstrained best-fit values in order to optimize the goodness of the constrained fit. With an increase in variation of l_p from its best-fit value, poorer fits are obtained at high frequencies (i.e., in the transition 2 and the high-frequency regions; see Fig. 7). A similar analysis is performed for other parameters $G_N, \varsigma, \langle L \rangle, \alpha_e$, and l_e with their corresponding fits as given in Appendix B. We here define the “insensitivity percentage” for a given parameter to be the maximum percentage variation in that parameter which can be allowed, while retaining an absolute maximum average fitting error (ε_{max} , defined in the note of Table II) of no more than 10% among all the four frequency regions. Note that a higher value of the insensitivity percentage implies a lower sensitivity of the fit to that parameter value. The insensitivity percentage can therefore be taken as an estimate of the “likely error” in that parameter value. We give the insensitivity percentages in Table III.

If high-frequency DWS data are not available, and fittings must be made to mechanical rheometric data alone, Fig. 11 shows that there is a larger insensitivity percentage

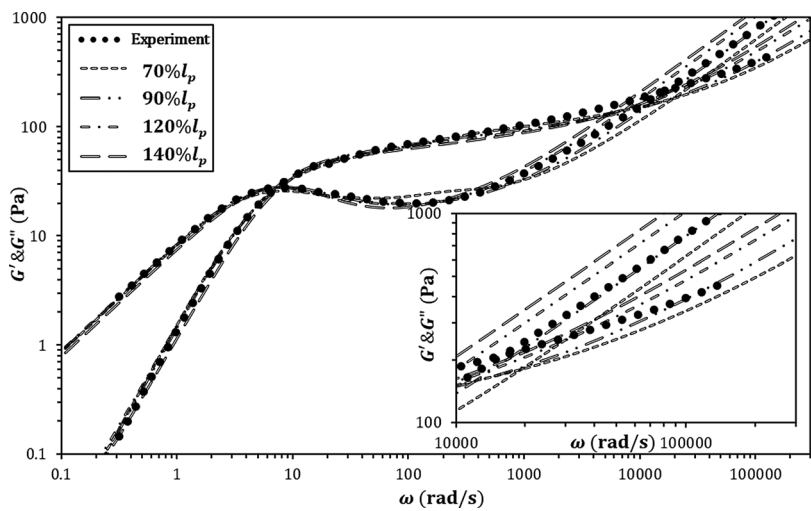


FIG. 10. Sensitivity of fits to the value of l_p for combined mechanical and DWS data in Fig. 9(d). Each curve results from a best fit of other parameters, with l_p constrained at a given percentage of the unconstrained best-fit value. The inset shows an enlarged view of the high-frequency fitting.

TABLE III. The summary of insensitivity percentages for micellar parameters for combined mechanical and DWS data of Fig. 9(d).

Parameter	Insensitivity percentage	Regions most sensitive to parameter	
		$G'(\omega)$	$G''(\omega)$
G_N	$\pm 10\%$	Transitions 1 and 2	Transition 1
ς	$\pm 20\%$ to $\pm 30\%$	Low frequency	Low frequency
$\langle L \rangle$	$\pm 30\%$	Low frequency, transition 1	Low frequency, transition 1
α_e	$\pm 2.5\%$ to $\pm 5\%$	Transitions 1 and 2	Transition 1
l_e	$\pm 5\%$ to $\pm 10\%$	Transitions 1 and 2	Transition 1, high frequency
l_p	$\pm 10\%$ to $\pm 20\%$	High frequency	Transition 2, high frequency

($\pm 20\% - \pm 30\%$) in persistence length l_p than is the case when fits are made to combined mechanical & DWS data, as in Fig. 10. As shown by Figs. 10 and 11, a larger l_p leads to a somewhat smaller ω_{min} causing the minimum in G'' to shift to a lower frequency, due to a greater contribution of bending modes [Eq. (10)] with an increase of l_p . An analytical expression for ω_{min} can be found in Granek (1994). This shift in ω_{min} and the corresponding shift in G''_{min} , if available from mechanical data, are in principle adequate to determine the value of l_p from mechanical data alone. However, compared to the large changes in the high-frequency data, to which the value of l_p is most sensitive, the effect of varying l_p on ω_{min} is modest (Figs. 10 and 11). Thus, the greater uncertainty in predicting l_p from mechanical data alone arises from the importance of the high-frequency data in securing an accurate estimate of l_p (see Fig. 10 at high frequencies). In addition, mechanical rheometric measurements are problematic at the upper range of their frequency, and fitting these data precisely sometimes require such a small l_p that deviations occur in fits to the lower-frequency mechanical data, as shown by the line for $60\%l_p$ in Fig. 11, which gives a best fit to the data near the minimum in G'' , but fails at lower frequency. Thus, DWS data should, if possible, be combined with the mechanical data for a more accurate and confident estimation of l_p , especially when the mechanical data do not reach frequencies high enough to resolve the local minimum in G'' , or the highest-frequency mechanical data cannot be well-fit without producing a poor fit at lower frequency.

While DWS data are very helpful to determine an accurate and trustworthy value of l_p , the data overlap between mechanical rheometry and DWS measurements becomes

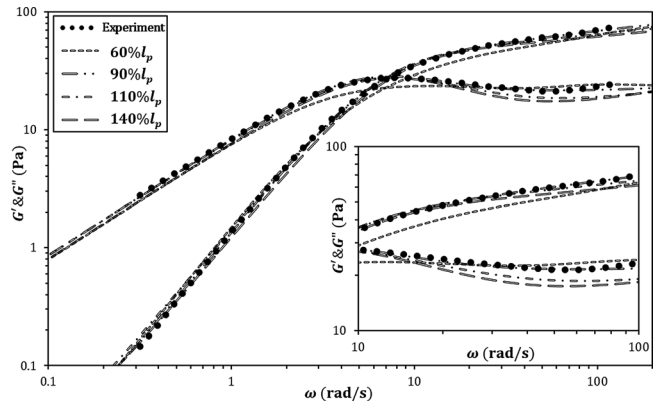


FIG. 11. The same as Fig. 10, except for mechanical data only shown in Fig. 9(b). The inset shows an enlarged view of the fitting near the minimum in G'' .

unsatisfactory in various cases, for instance, at low surfactant concentration. A vertical shift of the DWS data (which is typically high-frequency data) is often made in the literature to line up the DWS data with the mechanical data [Willenbacher *et al.* (2007); Oelschlaeger *et al.* (2009); Oelschlaeger *et al.* (2010);], but the validity of this remains unclear. A detailed discussion of the relationship between mechanical rheometry (macro-rheology) and particle-related DWS (microrheology) can be found in Buchanan *et al.* (2005).

C. Effect of salt

By effectively screening out the electrostatic interaction between surfactant charged headgroups, added salt greatly affects the rheological properties of micellar solutions, which is reflected in a sharp rise of the zero-shear viscosity (η_0) with increasing salt concentration (c_s) at low salt concentration, followed by a decrease in η_0 at high salt concentration. This nonmonotonic dependence of η_0 on c_s is referred to as a “salt curve.” The growth of WLMs and formation of micelle branches is believed to cause the increase and the subsequent decrease in viscosity, respectively [Khatory *et al.* (1993a)]. However, shifts of the salt curve are often observed when other additives (alcohols, perfumes, and organic solvents) are added to the surfactant-salt solutions because of their partial or complete incorporation into micelles [Fischer and Fieber (2009); Parker and Fieber (2013)].

In what follows, using our data-fitting procedure, we extract micellar parameters from the rheological data (G' and G'') for SLE1S/CAPB surfactant solutions at 11 wt. % of surfactants plus co-surfactants and 1 wt. % perfume (detailed components are given in Sec. III), with added NaCl varying from 0.63 wt. % to 2 wt. %. The salt curve and salt concentration-dependent micellar properties are shown in Fig. 12 (where the positions of the zero-shear viscosity maxima are indicated by arrows), while the measured mechanical data and the corresponding fitting curves can be found in Fig. 13. These data sets do not

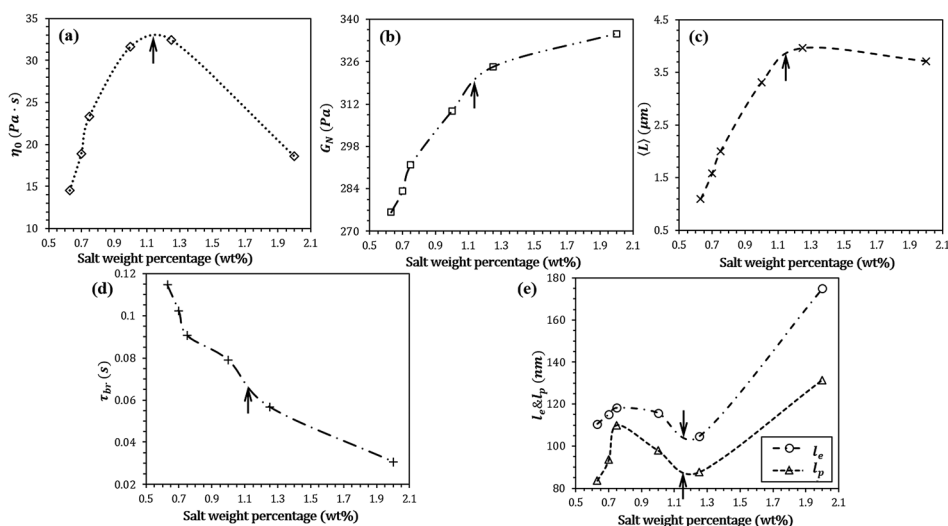


FIG. 12. The dependence of characteristic micellar parameters on salt weight percentage through fits to the experimental data for SLE1S/CAPB/NaCl surfactant solutions with perfume. (a) Zero-shear viscosity, η_0 ; (b) plateau modulus, G_N ; (c) average micelle length, $\langle L \rangle$; (d) average breakage time, τ_{br} ; and (e) micelle entanglement length, l_e and persistence length l_p . Notice the positions of the zero-shear viscosity maxima are indicated by arrows.

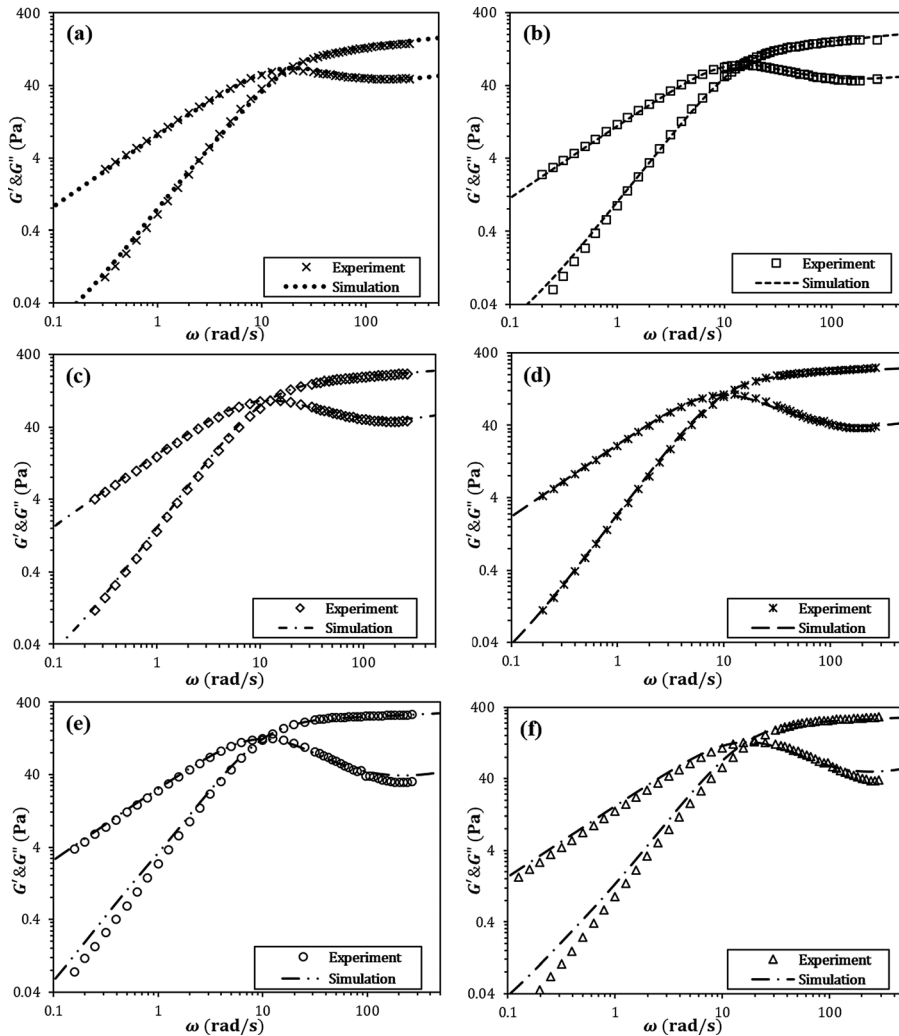


FIG. 13. Experimental and fitting results for SLEIS/CAPB/NaCl surfactant solutions with perfume and various salt weight fractions. (a) 0.63 wt. % NaCl; (b) 0.7 wt. % NaCl; (c) 0.75 wt. % NaCl; (d) 1.0 wt. % NaCl; (e) 1.25 wt. % NaCl; and (f) 2.0 wt. % NaCl. The fitting parameters are given in Fig. 12.

include DWS measurements, which limit somewhat the accuracy of the parameters extracted as we discussed above.

According to Fig. 12, both the plateau modulus G_N and the average breakage time $\bar{\tau}_{br}$ ($= \bar{\tau}_{rep}\zeta$, Eq. (3)) show monotonic dependences [Figs. 12(b) and 12(d)] on salt weight fraction: G_N increases with added salt while $\bar{\tau}_{br}$ decreases. This monotonic decrease of $\bar{\tau}_{br}$ with salt concentration has also been reported in the literature [Nakamura and Shikata (2006); Parker and Fieber (2013)]. According to our results, these solutions fall into the fast breakage regime with $\bar{\tau}_{br} \ll \bar{\tau}_{rep}$, and therefore $\zeta \ll 1$ [Eq. (3)], when the salt fraction is greater than 0.75 wt. %. An increase in average micelle length ($\langle L \rangle$) is also observed before the solution reaches the maximum on its salt curve, and beyond that, the apparent “length” $\langle L \rangle$ decreases slightly [Fig. 12(c)]. Since our method does not distinguish branched from linear micelles, the “micelle length” $\langle L \rangle$ at high salt concentration is only an apparent length, and its value more likely reflects the spacing between branch

points as much or even more than the micelle length [Khatory *et al.* (1993a)]. We are currently working on an extension of our simulation method to branched micelles, which should help overcome this limitation and may provide a quantitative interpretation on the rheological scaling behavior for G_N and other parameters as we did in Fig. 12. With a larger surfactant fraction (11 wt. %) than in the previous solution [6.67 wt. %, Fig. 9(a)], higher values of ω_{min} (the frequency where G'' reaches a local minimum) are observed [Fig. 13(a)–13(f)] causing poorer resolution of ω_{min} , from which micelle entanglement length (l_e) and persistence length (l_p) are extracted. Therefore, the possible errors in l_e and l_p for these samples are likely greater than for the mechanical data for the 6.67% SLE1S solution in Sec. VB, which we found had likely errors (or insensitivities) of 20%–30%. Thus, the nonmonotonic dependences of l_e and l_p on salt concentration given in Fig. 12(e) might be spurious, especially since l_p is expected to decrease monotonically with increasing salt concentration based on the predictions of Oelschlaeger *et al.* (2009, 2010). The poorer model fits in Figs. 13(e) and 13(f), especially at high frequencies may be due to the presence of branching in those samples.

D. Breakage mechanisms

Finally, in this section, the details of micellar breakage mechanisms and their effects on stress relaxation are discussed. As suggested by Turner and Cates (1992), three different micellar breakage schemes may occur in WLM solutions: Reversible scission, end-interchange, and bond-interchange, whose existence is studied by simulation and experimental work [Yamamoto and Hyodo (2005); Nakamura and Shikata (2006)]. Reversible scission is unimicellar, while the other two (end- and bond-interchange) are bimicellar and involve the formation of three- and four-arm intermediates, respectively. With the aid of pointer algorithm (Fig. 1), reversible scission can be modeled by three different sequences of breakage, rejoining and relaxation events, as shown in Fig. 14.

From Fig. 14, sequence 1 allows the total number of WLMs to fluctuate by randomly choosing a breakage or rejoining event after the relaxation, while sequences 2 and 3 are based on a regular cycle of breakage and rejoining. With a large enough ensemble, the above three sequences should give the same relaxation behavior, which is indeed shown in Fig. 15.

By extending our pointer algorithm to accommodate end- and bond-interchange (Fig. 16) with sequence 3, we find in Fig. 17 that pure end- and bond-interchange scheme

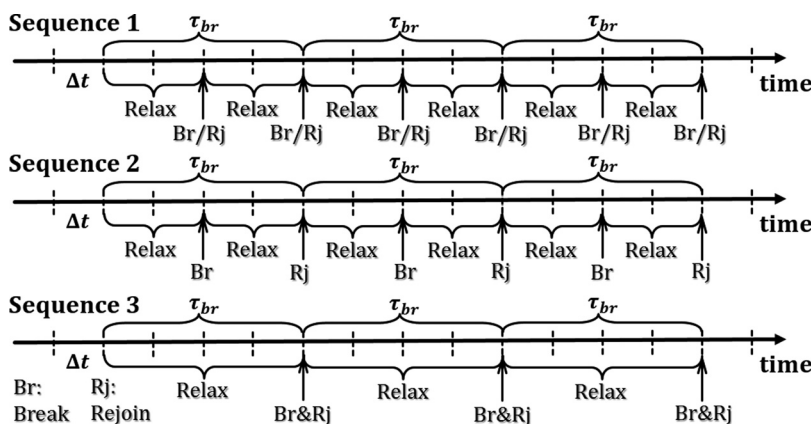


FIG. 14. Three different sequences in reversible scission scheme.

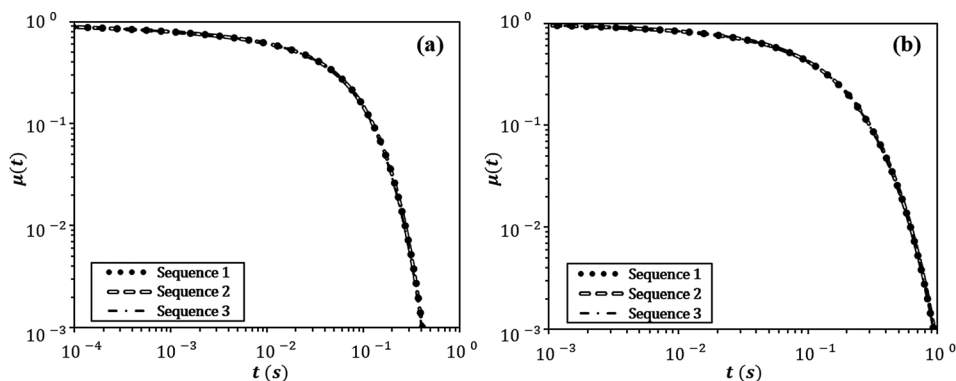


FIG. 15. Stress relaxation behaviors for reversible scission scheme with three different sequences, depicted in Fig. 14. (a) Reptation with CLFs; and (b) pure reptation (i.e., no CLFs).

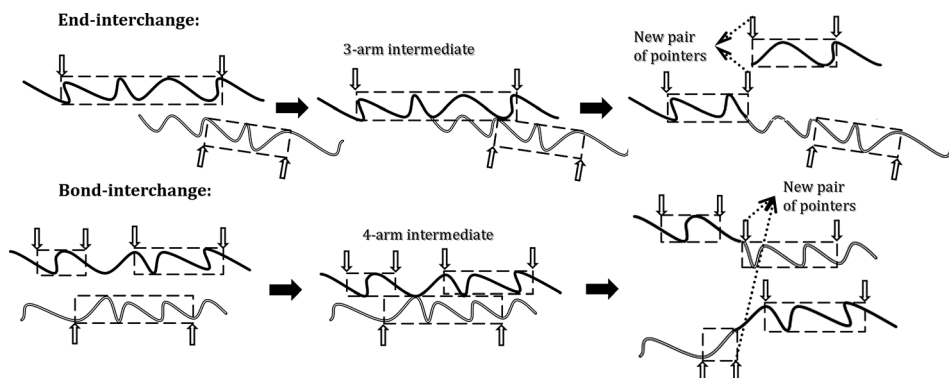


FIG. 16. Pointer algorithm with end-interchange and bond-interchange schemes.

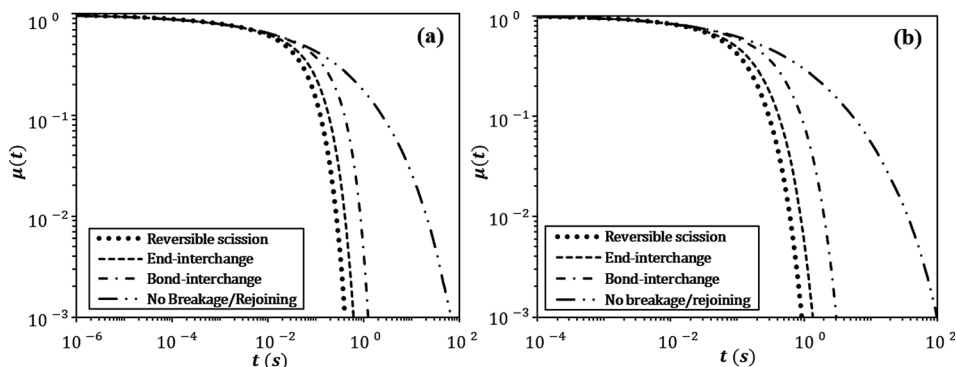


FIG. 17. Stress relaxation behaviors for different breakage schemes for fixed surfactant volume fraction with the sequence used as defined in the text. (a) Reptation with CLFs; and (b) pure reptation (i.e., no CLFs).

only produce a modest 10% and 30% increase, respectively, of the stress relaxation time [τ defined in Eq. (4)] for a high breakage rate ($\zeta = 0.05$) with fixed surfactant volume fraction ($\phi = 0.1$). Although the precise mechanism by which micelles break and rejoin should affect the dependence of micelle length and therefore viscoelasticity on surfactant concentration, for a fixed surfactant concentration considered here, such effects are not probed.

VI. CONCLUSIONS

We have established improved empirical relationships and an associated data-fitting procedure to allow quantitative estimation of micellar characteristic lengths (average micelle length $\langle L \rangle$, entanglement length l_e , and persistence length l_p) and times (average breakage time $\bar{\tau}_{br}$ and reptation time $\bar{\tau}_{rep}$) to be extracted from rheological data using our recently developed simulation method for entangled WLM solutions. We were able to obtain fits to G' and G'' data with less than 5% absolute average deviation over a six-decade frequency range, including high-frequency data obtained from DWS. A comparison of fitted micellar parameters was made between DWS data and mechanical rheometric data for WLM solution, and this indicates the importance of low-frequency data in estimating the plateau modulus G_N , the dimensionless breakage rate ζ , and the semi-flexibility coefficient α_e . The accuracy of our simulation method was demonstrated by sensitivity studies for different micellar parameters. By applying our method to examine effects of added salt concentration, we observed monotonic and nonmonotonic dependences of different micellar parameters on salt concentration, as well as poorer fits at high salt weight fraction where branched micelles predominate. Finally, three different micellar breakage schemes (reversible scission, end-interchange, and bond-interchange) and their rather modest effect on the stress relaxation for fixed surfactant concentration were discussed.

ACKNOWLEDGMENTS

The authors acknowledge support from the National Science Foundation (NSF) (under Grant Nos. CBET-0853662 and DMR-1403335) and discussions with Mike Cates, Karsten Vogtt, and Gregory Beaucage of University of Cincinnati, and Shawn McConaughy of Procter & Gamble. Any opinions, findings, and conclusions or recommendations expressed in this material are those of the authors and do not necessarily reflect the views of NSF.

APPENDIX A: DETAILED DATA-FITTING PROCEDURE

The data-fitting flowchart (Fig. 18) as well as equations used to update the parameters (G_N , ζ , $\bar{\tau}_{rep}$, Z , l_p) from one iteration to the next are given in this Appendix.

1. l_p

According to Eq. (10), l_p relates to the high-frequency rheological behavior of WLM solutions through its scaling effect on both the magnitudes of $G'(\omega)$ and $G''(\omega)$ and the “upturn” frequency (ω_{min}), i.e., $G'(\omega)$ and $G''(\omega) \sim l_p^{1.25}$ and $\omega_{min} \sim \tau_p^{-1} \sim l_p^{-3}$. The former scaling implies that if the fitted high-frequency modulus is higher than the experimental one [which means that the average deviation for region 3 and 4 in Eq. (15) is

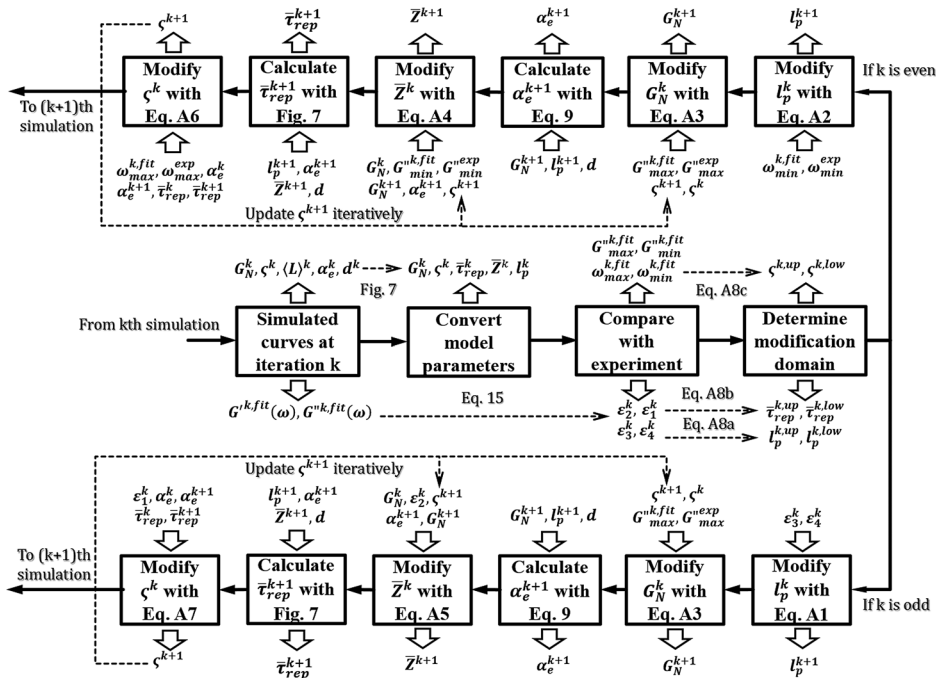


FIG. 18. Flowchart showing data-fitting procedure.

positive], then one needs to reduce l_p . The latter scaling implies that if the fitted upturn frequency is higher than the experimental value, one needs to increase l_p . From these scaling rules given above, we specify the following two ways, one “regional” (i.e., tuning specific micellar parameters based on the average deviations over a particular frequency region in Fig. 7) and the other “local,” (i.e., tuning micellar parameters based on the difference between experimental and simulation results for specific frequencies in Fig. 3) to update l_p at iteration k

$$l_p^{k+1} = l_p^k \exp(-0.8\epsilon_{avg}^k), \quad \begin{cases} \text{If } N_4 \neq 0, & \epsilon_{avg}^k = (\epsilon_3^k + \epsilon_4^k)/2 \\ \text{Otherwise,} & \epsilon_{avg}^k = \epsilon_3^k, \end{cases} \quad (\text{A1})$$

$$l_p^{k+1} = l_p^k \sqrt[3]{\omega_{min}^{k,fit}/\omega_{min}^{exp}}. \quad (\text{A2})$$

As depicted in Fig. 18, Eq. (A1) is used in odd-numbered iteration steps, and Eq. (A2) in even-numbered steps.

2. G_N and α_e

Since G_N can be treated as the scaling factor for the low frequency behavior, as shown in Eq. (14c), it can therefore be updated by comparing the simulated value of $G_N^{k,fit}$ with the experimental one, G_N^{exp}

$$G_N^{k+1} = \frac{G_N^{exp}}{G_N^{k,fit}/G_N^k - 0.0657 \log(\zeta^k/\zeta^{k+1})}, \quad (\text{A3})$$

where ς^{k+1} is determined iteratively with its value updated by Eqs. (A6) or (A7) after modifications for all the other parameters. We need to account for the value of ς when adjusting G_N , because G''_{max} shifts with the logarithm of ς , as we noted earlier [Eq. (14c)]. With the prior knowledge of the micelle diameter (d) and with the updated parameters (G_N^{k+1}, l_p^{k+1}) from above steps, the semiflexibility coefficient α_e^{k+1} for the next round of iteration can be obtained from Eq. (9), and is used in the next step of the simulation. As shown in Fig. 18, Eq. (A3) is used in both odd- and even-number iteration steps.

3. $\bar{Z}, \langle L \rangle, \langle L_t \rangle$, and $\bar{\tau}_{rep}$

Based on Eq. (14b), which gives the dependence of G''_{min}/G_N on \bar{Z} , with known α_e^{k+1} and G_N^{k+1} , regardless of prefactors that weakly depend on ς , \bar{Z} can be corrected as follows:

$$\begin{aligned} \text{If } \alpha_e^{k+1} > 1.5 \text{ and } \bar{Z}^{k+1} \leq \bar{Z}_c(\varsigma^{k+1}), \quad \bar{Z}^{k+1} &= \bar{Z}^k \frac{G''_{min}^{k,fit} G_N^{k+1}}{G''_{min}^{exp} G_N^k}, \\ \text{If } \alpha_e^{k+1} > 1.5 \text{ and } \bar{Z}^{k+1} > \bar{Z}_c(\varsigma^{k+1}), \quad \bar{Z}^{k+1} &= \bar{Z}^k \left(\frac{G''_{min}^{k,fit} G_N^{k+1}}{G''_{min}^{exp} G_N^k} \right)^{4/3}, \\ \text{If } \alpha_e^{k+1} < 1.5, \quad \bar{Z}^{k+1} &= \bar{Z}^k \left(\frac{G''_{min}^{k,fit} G_N^{k+1}}{G''_{min}^{exp} G_N^k} \right)^5. \end{aligned} \quad (\text{A4})$$

Instead of using the ratio of simulated to experimental modulus at the specific frequency where G'' is minimum, the overall fit in the transition 1 region (see Fig. 7) can also be used to modify \bar{Z} . To do this, we simply replace $G''_{min}^{k,fit}/G''_{min}^{exp}$ with $\exp(\varepsilon_2^k)$ in the above equation, which yields

$$\begin{aligned} \text{If } \alpha_e^{k+1} > 1.5 \text{ and } \bar{Z}^{k+1} \leq \bar{Z}_c(\varsigma^{k+1}), \quad \bar{Z}^{k+1} &= \bar{Z}^k \exp(\varepsilon_2^k) \frac{G_N^{k+1}}{G_N^k}, \\ \text{If } \alpha_e^{k+1} > 1.5 \text{ and } \bar{Z}^{k+1} > \bar{Z}_c(\varsigma^{k+1}), \quad \bar{Z}^{k+1} &= \bar{Z}^k \exp\left(\frac{4}{3} \varepsilon_2^k\right) \left(\frac{G_N^{k+1}}{G_N^k} \right)^{4/3}, \\ \text{If } \alpha_e^{k+1} < 1.5, \quad \bar{Z}^{k+1} &= \bar{Z}^k \exp\left(\frac{4}{3} \varepsilon_2^k\right) \left(\frac{G_N^{k+1}}{G_N^k} \right)^5. \end{aligned} \quad (\text{A5})$$

Equations (A4) and (A5) are used in even- and odd-numbered iteration steps, respectively, according to Fig. 18. According to Fig. 8, with known l_p, α_e and d , $\bar{\tau}_{rep}$ is related to \bar{Z} through $\langle L \rangle$ and $\langle L_t \rangle$. Thus, once \bar{Z} is updated, $\langle L \rangle^{k+1}, \langle L_t \rangle^{k+1}, \bar{\tau}_{rep}^{k+1}$ can be calculated from Eqs. (2), (7), (8), and (11).

4. ς

According to Eq. (14a), corrections of ς can be made by ε_1^k or $\omega_{max}^{k,fit}/\omega_{max}^{exp}$ with known α_e^{k+1} and $\bar{\tau}_{rep}^{k+1}$

$$\varsigma^{k+1} = \varsigma^k \left[\frac{\omega_{max}^{k,fit} \bar{\tau}_{rep}^k}{\omega_{max}^{exp} \bar{\tau}_{rep}^{k+1}} \left(\frac{\alpha_e^{k+1}}{\alpha_e^k} \right)^3 \right]^{3/2}. \quad (\text{A6})$$

Again, if we wish to update ς using fitting deviation over a range of frequencies, we can replace $\omega_{max}^{k,fit}/\omega_{max}^{exp}$ with $\exp(2/3\varepsilon_1^k)$, giving

$$\varsigma^{k+1} = \varsigma^k \exp(\varepsilon_1^k) \left[\frac{\bar{\tau}_{rep}^k}{\bar{\tau}_{rep}^{k+1}} \left(\frac{\alpha_e^{k+1}}{\alpha_e^k} \right)^3 \right]^{3/2}. \quad (\text{A7})$$

Equation (A6) is used in even-numbered iterations and Eq. (A7) in odd-numbered ones.

5. Limits of parameter modification

To avoid instability during the iteration, we limit the extent to which parameters ($l_p, \bar{\tau}_{rep}, \varsigma$) can change in a single iteration. The upper and lower bound for modifications are given in Eq. (A8). As an example, the evolution of the allowed modification range for l_p is illustrated below

$$l_p^{k,up} = l_p^k \exp(0.8|\varepsilon_{avg}^k|), \quad l_p^{k,low} = l_p^k \exp(-0.8|\varepsilon_{avg}^k|), \quad (\text{A8a})$$

$$\bar{\tau}_{rep}^{k,up} = \bar{\tau}_{rep}^k \exp\left(\frac{2}{3}|\varepsilon_1^k|\right), \quad \bar{\tau}_{rep}^{k,low} = \bar{\tau}_{rep}^k \exp\left(-\frac{2}{3}|\varepsilon_1^k|\right), \quad (\text{A8b})$$

$$\text{If } \omega_{max}^{k,fit} > \omega_{max}^{exp}, \quad \varsigma^{k,up} = \varsigma^k \left(\frac{\omega_{max}^{k,fit}}{\omega_{max}^{exp}} \right)^{3/2}, \quad \varsigma^{k,low} = \varsigma^k \left(\frac{\omega_{max}^{k,fit}}{\omega_{max}^{exp}} \right)^{-3/2} \quad (\text{A8c})$$

$$\text{Otherwise, } \varsigma^{k,up} = \varsigma^k \left(\frac{\omega_{max}^{exp}}{\omega_{max}^{k,fit}} \right)^{3/2}, \quad \varsigma^{k,low} = \varsigma^k \left(\frac{\omega_{max}^{exp}}{\omega_{max}^{k,fit}} \right)^{-3/2}.$$

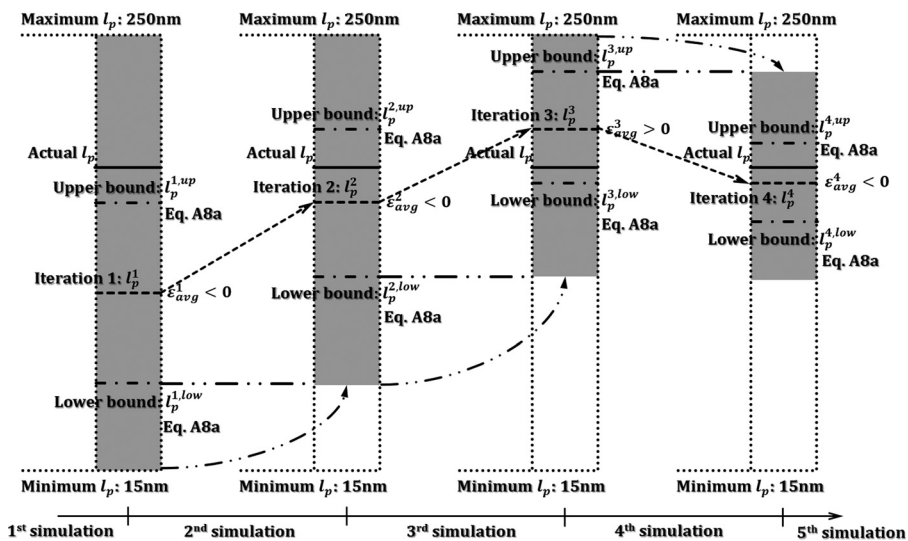


FIG. 19. Evolution of the allowed modification range for l_p represented by gray regions.

APPENDIX B: SENSITIVITY STUDIES FOR PARAMETERS d , G_N , ς , $\langle L \rangle$, α_e , AND l_e

The estimates of parameters and associated fitting curves for sensitivity studies to parameters d , G_N , ς , $\langle L \rangle$, α_e , l_e are shown in Tables IV–IX and Figs. 20–25 below.

TABLE IV. Estimated parameters from best fits in Fig. 20 with different imposed values of d .

Parameters	$d = 3 \text{ nm}$	$d = 3.5 \text{ nm}$	$d = 4 \text{ nm}$	$d = 4.5 \text{ nm}$
$G_N \text{ (Pa)}$	108	104	115	108
ς	0.65	0.63	1.82	1.8
$\langle L \rangle \text{ (}\mu\text{m)}$	2.2	2.03	1.59	1.36
α_e	2.162	1.682	1.363	1.182
$l_e \text{ (nm)}$	147	164	153	156
$l_p \text{ (nm)}$	68	98	112	132

TABLE V. Parameter values obtained by best fitting rheological data, for imposed values of G_N .

Parameters	80% G_N	85% G_N	90% G_N	95% G_N	Best-fit G_N	105% G_N	110% G_N	115% G_N	120% G_N
$G_N \text{ (Pa)}$	92	97.75	103.5	109.25	115	120.75	126.5	132.25	138
ς	1.74	1.71	1.99	2.18	1.82	1.71	1.23	1.70	1.48
$\langle L \rangle \text{ (}\mu\text{m)}$	1.64	1.64	1.59	1.54	1.59	1.59	1.72	1.61	1.60
α_e	1.421	1.375	1.387	1.371	1.363	1.361	1.333	1.347	1.365
$l_e \text{ (nm)}$	179	176	165	159	153	147	144	136	131
$l_p \text{ (nm)}$	126	128	119	116	112	108	108	101	96
$\varepsilon_{max} \text{ (\%)}^a$	19.1	13	9.4	5.8	4.1	4.5	9.6	11.8	16.8

^aNote that by varying G_N from its unconstrained best-fit value, the maximum average fitting error (ε_{max} , defined in the notes of Table II) occurs in transition 1 region (see Fig. 7), as shown by Fig. 21.

TABLE VI. The same as Table V, except for imposed values of ς .

Parameters	20% ς	40% ς	60% ς	80% ς	Best-fit ς	120% ς	140% ς	160% ς	180% ς
$G_N \text{ (Pa)}$	86.8	91.4	97.1	112.8	115	117	119.4	118	122.1
ς	0.36	0.73	1.1	1.46	1.82	2.18	2.55	2.91	3.28
$\langle L \rangle \text{ (}\mu\text{m)}$	1.33	1.39	1.42	1.63	1.59	1.53	1.59	1.59	1.62
α_e	1.418	1.372	1.372	1.375	1.363	1.404	1.37	1.38	1.352
$l_e \text{ (nm)}$	190	188	177	154	153	146	148	149	149
$l_p \text{ (nm)}$	134	137	129	112	112	104	108	108	108
$\varepsilon_{max} \text{ (\%)}^a$	>100	90	58	4.9	4.1	8.6	25	29.3	36.6

^aNote that for imposed values of ς , ε_{max} occurs in the low frequency region, as shown by Fig. 22.

TABLE VII. The same as Table V, except for imposed values of $\langle L \rangle$.

Parameters	40% $\langle L \rangle$	55% $\langle L \rangle$	70% $\langle L \rangle$	85% $\langle L \rangle$	Best-fit $\langle L \rangle$	115% $\langle L \rangle$	130% $\langle L \rangle$	145% $\langle L \rangle$	160% $\langle L \rangle$
$G_N \text{ (Pa)}$	80	111.5	116	112	115	108	104.5	100	95.5
ς	13.03	9.42	5.95	3.17	1.82	1.04	0.60	0.43	0.28
$\langle L \rangle \text{ (}\mu\text{m)}$	0.636	0.875	1.11	1.35	1.59	1.83	2.07	2.31	2.54
α_e	1.626	1.396	1.413	1.391	1.363	1.402	1.378	1.39	1.391
$l_e \text{ (nm)}$	174	155	147	153	153	157	164	171	178
$l_p \text{ (nm)}$	107	111	104	110	112	112	119	123	128
$\varepsilon_{max} \text{ (\%)}^a$	32.6	26.3	9.8	6.7	4.1	6.4	7.8	11.4	15.8

^aNote that for imposed values of $\langle L \rangle$, ε_{max} occurs in low frequency and transition 1 region, as shown by Fig. 23.

TABLE VIII. The same as Table V, except for imposed values of α_e .

Parameters	90% α_e	92.5% α_e	95% α_e	97.5% α_e	Best-fit α_e	102.5% α_e	105% α_e	107.5% α_e	110% α_e
G_N (Pa)	163.5	145	135	127	115	115.5	110.5	106.5	102
ζ	1.11	2.47	2.49	1.24	1.82	1.94	1.9	2.08	2.24
$\langle L \rangle$ (μm)	1.75	1.57	1.62	1.7	1.59	1.58	1.59	1.58	1.57
α_e	1.227	1.261	1.295	1.329	1.363	1.397	1.431	1.465	1.499
l_e (nm)	123	130	140	144	153	149	150	152	154
l_p (nm)	100	103	108	108	112	107	105	104	103
ε_{max} (%) ^a	43.9	40.7	38.4	9.8	4.1	7.3	9.7	12.1	15

^aNote that for imposed values of α_e , there is no specific frequency region where ε_{max} always occurs, as shown by Fig. 24.

TABLE IX. The same as Table V, except for imposed values of l_e .

Parameters	70% l_e	80% l_e	90% l_e	Best-fit l_e	110% l_e	120% l_e	130% l_e	140% l_e	150% l_e
G_N (Pa)	180	150	132	115	107.5	98.5	90	82	75.5
ζ	0.63	2.09	1.51	1.82	2.11	1.86	2.16	2.1	2.04
$\langle L \rangle$ (μm)	2	1.81	1.64	1.59	1.45	1.49	1.4	1.27	1.17
α_e	1.342	1.36	1.343	1.363	1.325	1.319	1.32	1.331	1.349
l_e (nm)	106	122	137	153	167	182	198	213	228
l_p (nm)	79	90	102	112	126	138	150	160	169
ε_{max} (%) ^a	48.1	23.6	12.1	4.1	6.4	9.9	15.1	18.2	21

^aNote that for imposed values of l_e , there is no specific frequency region where ε_{max} always occurs, as shown by Fig. 25.

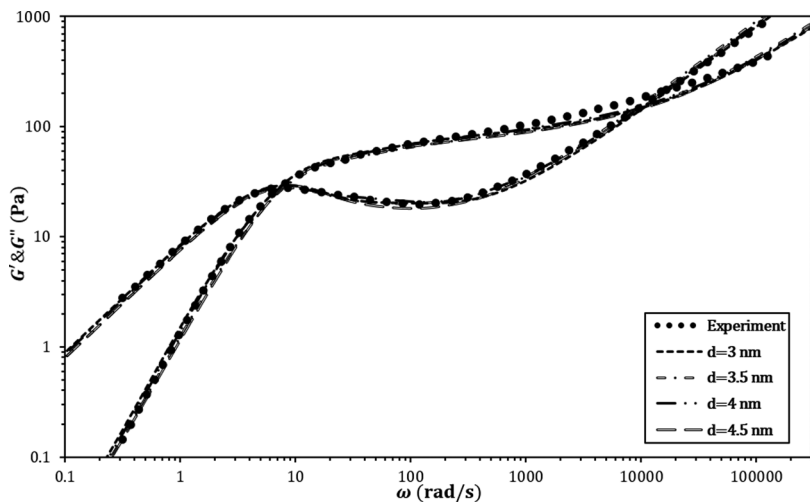


FIG. 20. Best fits for WLM solution (6.67 wt. % SLE1S, 3.10 wt. % NaCl with solvent viscosity $\eta_s = 0.9$ cP at 25°C) with different imposed value of d showing the inability of rheology to determine micelle diameter.

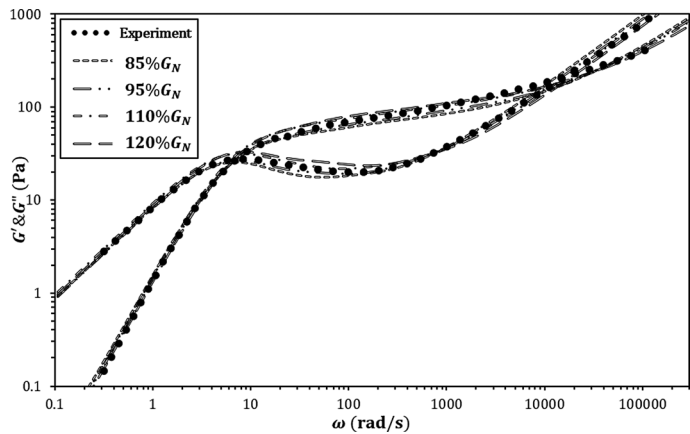


FIG. 21. Fitting results showing sensitivity of best fits to imposed values of G_N with $d = 4$ nm for WLM solution (6.67 wt. % SLE1S, 3.10 wt. % NaCl with solvent viscosity $\eta_s = 0.9$ cP at 25 °C).

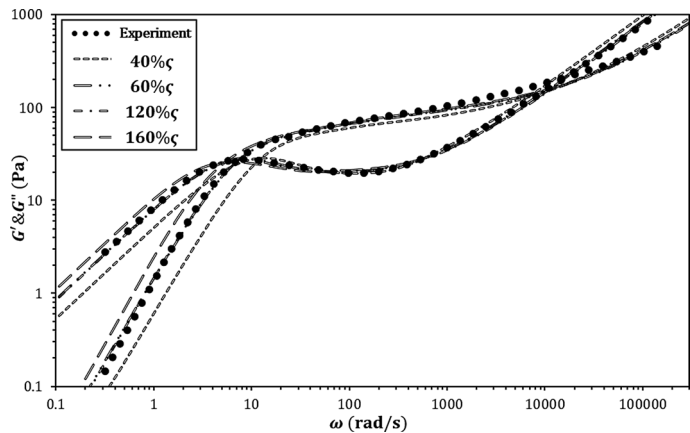


FIG. 22. The same as Fig. 21, except that variation is made in ζ .

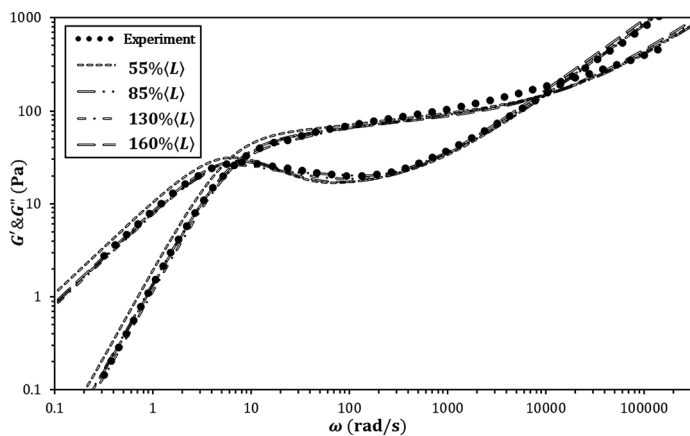


FIG. 23. The same as Fig. 21, except that variation is made in $\langle L \rangle$.

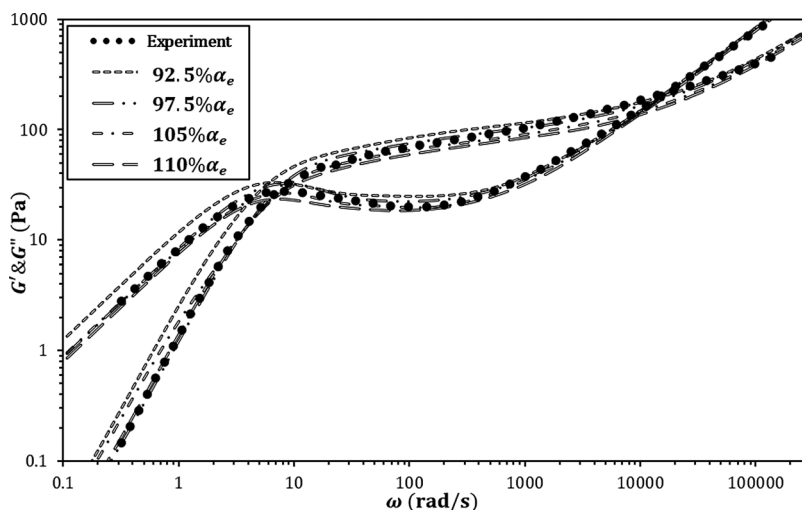


FIG. 24. The same as Fig. 21, except that variation is made in α_e .

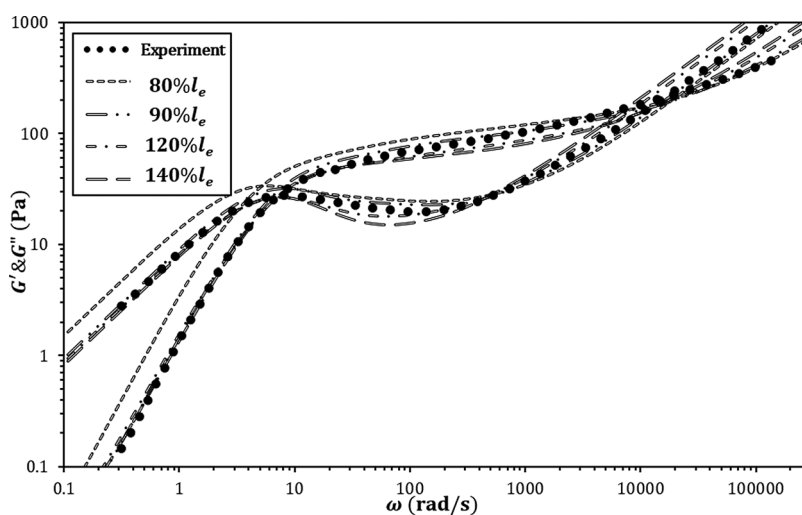


FIG. 25. The same as Fig. 21, except that variation is made in l_e .

References

- Babintsev, I. A., L. T. Adzhemyan, and A. K. Shchekin, "Kinetics of micellisation and relaxation of cylindrical micelles described by the difference Becker-Döring equation," *Soft Matter* **10**, 2619–2631 (2014).
- Baccile, N., F. Babonneau, J. Jestin, G. Pehau-Arnaudet, and I. V. Bogaert, "Unusual, pH-induced, self-assembly of sophorolipid biosurfactants," *ACS Nano* **6**, 4763–4776 (2012).
- Beaumont, J., N. Louvet, T. Divoux, M.-A. Fardin, H. Bodiguel, S. Lerouge, S. Manneville, and A. Colin, "Turbulent flows in highly elastic wormlike micelles," *Soft Matter* **9**, 735–749 (2013).
- Beck, J. S., J. C. Vartuli, W. J. Roth, M. E. Leonowicz, C. T. Kresge, K. D. Schmitt, C. T.-W. Chu, D. H. Olson, E. W. Sheppard, S. B. McCullen, J. B. Higgins, and J. L. Schlenker, "A new family of mesoporous molecular sieves prepared with liquid crystal templates," *J. Am. Chem. Soc.* **114**, 10834–10843 (1992).
- Bernheim-Groswasser, A., E. Wachtel, and Y. Talmon, "Micellar growth, network formation, and criticality in aqueous solutions of the nonionic surfactant $C_{12}E_5$," *Langmuir* **16**, 4131–4140 (2000).

- Buchanan, M., M. Ataknorrani, J. F. Palierne, and C. F. Schmidt, "Comparing macrorheology and one- and two-point microrheology in wormlike micelle solutions," *Macromolecules* **38**, 8840–8844 (2005).
- Candau, S. J., E. Hirsch, R. Zana, and M. Delsanti, "Rheological properties of semidilute and concentrated aqueous solutions of cetyltrimethylammonium bromide in the presence of potassium bromide," *Langmuir* **5**, 1225–1229 (1989).
- Cates, M. E., "Reptation of living polymers: Dynamics of entangled polymers in the presence of reversible chain-scission reaction," *Macromolecules* **20**, 2289–2296 (1987).
- Cates, M. E., "Dynamics of living polymers and flexible surfactant micelles: Scaling laws for dilution," *J. Phys.* **49**, 1593–1600 (1988).
- Cates, M. E., and S. J. Candau, "Statics and dynamics of worm-like surfactant micelles," *J. Phys.: Condense Matter* **2**, 6869–6892 (1990).
- Chen, W., P. D. Butler, and L. J. Magid, "Incorporating intermicellar interactions in the fitting of SANS data from cationic wormlike micelles," *Langmuir* **22**, 6539–6548 (2006).
- Croce, V., T. Cosgrove, G. Maitland, T. Hughes, and G. Karlsson, "Rheology, cryogenic transmission electron spectroscopy, and small-angle neutron scattering of highly viscoelastic wormlike micellar solutions," *Langmuir* **19**, 8536–8541 (2003).
- Dealy, J. M., and R. G. Larson, *Structure and Rheology of Molten Polymers: From Structure to Flow Behavior and Back Again* (Hanser Gardner, Cincinnati, 2005).
- de Gennes, P. G., *Scaling Concepts in Polymer Physics* (Cornell University, New York, 1979).
- de Silva, M. A., E. Weinzaepfel, H. Afifi, J. Eriksson, I. Grillo, M. Valero, and C. A. Dreiss, "Tuning the viscoelasticity of nonionic wormlike micelles with β -cyclodextrin derivatives: A highly discriminative process," *Langmuir* **29**, 7697–7708 (2013).
- des Cloizeaux, J., "Double reptation vs. simple reptation in polymer melts," *Europhys. Lett.* **5**, 437–442 (1988).
- Doi, M., and S. F. Edwards, *The Theory of Polymer Dynamics* (Clarendon, Oxford, 1986).
- Fischer, E., W. Fieber, C. Navarro, H. Sommer, D. Benczédi, M. I. Velazco, and M. Schönhoff, "Partitioning and localization of fragrances in surfactant mixed micelles," *J. Surfactant Deterg.* **12**, 73–84 (2009).
- Galvan-Miyoshi, J., J. Delgado, and R. Castillo, "Diffusing wave spectroscopy in Maxwellian fluids," *Eur. Phys. J. E* **26**, 369–377 (2008).
- Gittes, F., and F. C. MacKintosh, "Dynamic shear modulus of a semiflexible polymer network," *Phys. Rev. E* **58**, 1241–1244 (1998).
- Granek, R., "Dip in $G''(\omega)$ of polymer melts and semidilute solutions," *Langmuir* **10**, 1627–1629 (1994).
- Granek, R., and M. E. Cates, "Stress relaxation in living polymers: Results from a Poisson renewal model," *J. Chem. Phys.* **96**, 4758–4767 (1992).
- Ilgenfritz, G., R. Schneider, E. Grell, E. Lewitzki, and H. Ruf, "Thermodynamic and kinetic study of the sphere-to-rod transition in nonionic micelles: Aggregation and stress relaxation in $C_{14}E_8$ and $C_{16}E_8/H_2O$ systems," *Langmuir* **20**, 1620–1630 (2004).
- Imae, T., and S. Ikeda, "Sphere-rod transition of micelles of tetradecyltrimethyl-ammonium halides in aqueous sodium halide solutions and flexibility and entanglement of long rodlike micelles," *J. Phys. Chem.* **90**, 5216–5223 (1986).
- James, G. K., and J. Y. Walz, "Experimental investigation of the effects of ionic micelles on colloidal stability," *J. Colloid Interface Sci.* **418**, 283–291 (2014).
- Jensen, G. V., R. Lund, J. Gummel, M. Monkenbusch, T. Narayanan, and J. S. Pedersen, "Direct observation of the formation of surfactant micelles under nonisothermal conditions by synchrotron SAXS," *J. Am. Chem. Soc.* **135**, 7214–7222 (2013).
- Kalur, G. C., B. D. Frounfelker, B. H. Cipriano, A. I. Norman, and S. R. Raghavan, "Viscosity increase with temperature in cationic surfactant solutions due to the growth of wormlike micelles," *Langmuir* **21**, 10998–11004 (2005).
- Ketner, A. M., R. Kumar, T. S. Davies, P. W. Elder, and S. R. Raghavan, "A simple class of photorheological fluids: Surfactant solutions with viscosity tunable by light," *J. Am. Chem. Soc.* **129**, 1553–1559 (2007).
- Khatory, A., F. Kern, F. Lequeux, J. Appell, G. Porte, N. Morie, A. Ott, and W. Urbach, "Entangled versus multiconnected network of wormlike micelles," *Langmuir* **9**, 933–939 (1993a).

- Khatory, A., F. Lequeux, F. Kern, and S. J. Candau, "Linear and nonlinear viscoelasticity of semidilute solutions of wormlike micelles at high salt content," *Langmuir* **9**, 1456–1464 (1993b).
- Kuperkar, K., L. Abezgauz, D. Danino, G. Verma, P. A. Hassan, V. K. Aswal, D. Varade, and P. Bahadur, "Viscoelastic micellar water/CTAB/NaNO₃ solutions: Rheology, SANS and cryo-TEM analysis," *J. Colloid Interface Sci.* **323**, 403–409 (2008).
- Kusano, T., H. Iwase, T. Yoshimura, and M. Shibayama, "Structural and rheological studies on growth of salt-free wormlike micelles formed by star-type trimeric surfactants," *Langmuir* **28**, 16798–16806 (2012).
- Larson, R. G., "The lengths of threadlike micelles inferred from rheology," *J. Rheol.* **56**, 1363–1374 (2012).
- Likhtman, A. E., and T. C. B. McLeish, "Quantitative theory for linear dynamics of linear entangled polymers," *Macromolecules* **35**, 6332–6343 (2002).
- Lu, Y., T. Zhou, Q. Fan, J. Dong, and X. Li, "Light-responsive viscoelastic fluids based on anionic wormlike micelles," *J. Colloids Interface Sci.* **412**, 107–111 (2013).
- Marignan, J., J. Appell, P. Bassereau, G. Porte, and R. P. May, "Local structures of the surfactant aggregates in dilute solutions deduced from small angle neutron scattering patterns," *J. Phys.* **50**, 3553–3566 (1989).
- Milner, S. T., and T. C. B. McLeish, "Parameter-free theory for stress relaxation in star polymer melts," *Macromolecules* **30**, 2159–2166 (1997).
- Milner, S. T., and T. C. B. McLeish, "Reptation and contour-length fluctuations in melts of linear polymers," *Phys. Rev. Lett.* **81**, 725–728 (1998).
- Morse, D. C., "Viscoelasticity of concentrated isotropic solutions of semiflexible polymers: 1. Model and stress tensor," *Macromolecules* **31**, 7030–7043 (1998a).
- Morse, D. C., "Viscoelasticity of concentrated isotropic solutions of semiflexible polymers: 2. Linear response," *Macromolecules* **31**, 7044–7067 (1998b).
- Nakamura, K., and T. Shikata, "Threadlike micelle formation of anionic surfactants in aqueous solution," *Langmuir* **22**, 9853–9859 (2006).
- Nettesheim, F., and N. J. Wagner, "Fast dynamics of wormlike micellar solutions," *Langmuir* **23**, 5267–5269 (2007).
- Oelschlaeger, C., M. Schopferer, F. Scheffold, and N. Willenbacher, "Linear-to-branched micelles transition: A rheometry and diffusing wave spectroscopy (DWS) study," *Langmuir* **25**, 716–723 (2009).
- Oelschlaeger, C., P. Suwita, and N. Willenbacher, "Effect of counterion binding efficiency on structure and dynamics of wormlike micelles," *Langmuir* **26**, 7045–7053 (2010).
- Padia, N. F., M. Yaseen, B. Gore, S. Rogers, G. Bell, and J. R. Lu, "Influence of molecular structure of nonionic C_nEm surfactant micelles," *J. Phys. Chem. B* **118**, 179–188 (2014).
- Parker, A., and W. Fieber, "Viscoelasticity of anionic wormlike micelles: Effects of ionic strength and small hydrophobic molecules," *Soft Matter* **9**, 1203–1213 (2013).
- Pérez, S. V., A. F. Olea, and M. P. Gárate, "Formation and morphology of reverse micelles formed by nonionic surfactants in "dry" organic solvents," *Curr. Top. Med. Chem.* **14**, 774–780 (2014).
- Porte, G., J. Appell, and Y. Poggi, "Experimental investigations on the flexibility of elongated cetylpyridinium bromide micelles," *J. Phys. Chem.* **84**, 3105–3110 (1980).
- Razak, N. A., and M. N. Khan, "Determination of flow activation energy at viscosity maximum for spherical and wormlike micelles of different lengths and flexibility," *Rheol. Acta* **52**, 927–937 (2013).
- Romano, S. D., and D. H. Kurlat, "Rheological measurements in titania gels synthesized from reverse micelles," *Chem. Phys. Lett.* **323**, 93–97 (2000).
- Shi, H., W. Ge, Y. Wang, B. Fang, J. T. Huggins, T. A. Russell, Y. Talmon, D. J. Hart, and J. L. Zakin, "A drag reducing surfactant threadlike micelle system with unusual rheological responses to pH," *J. Colloid Interface Sci.* **418**, 95–102 (2014).
- Shikata, T., S. J. Dahman, and D. S. Pearson, "Rheo-optical behavior of wormlike micelles," *Langmuir* **10**, 3470–3476 (1994).
- Siriwatwechakul, W., T. LaFleur, R. K. Prud'homme, and P. Sullivan, "Effects of organic solvents on the scission energy of rodlike micelles," *Langmuir* **20**, 8970–8974 (2004).
- Sreejith, L., S. Parathakkat, S. M. Nair, S. Kumar, G. Varma, P. A. Hassan, and Y. Talmon, "Octanol-triggered self-assemblies of the CTAB/KBr system: A microstructural study," *J. Phys. Chem. B* **115**, 464–470 (2011).

- Tuminello, W. H., "Molecular-weight polydispersity effects on the viscoelasticity of entangled linear polymers," *Polym. Eng. Sci.* **26**, 1339–1347 (1986).
- Turner, M. S., and M. E. Cates, "Linear viscoelasticity of living polymers: A quantitative probe of chemical relaxation times," *Langmuir* **7**, 1590–1594 (1991).
- Turner, M. S., and M. E. Cates, "Linear viscoelasticity of wormlike micelles: A comparison of micellar reaction kinetics," *J. Phys.* **2**, 503–519 (1992).
- Wang, Z., X. Chen, and R. G. Larson, "Comparing tube models for predicting the linear rheology of branched polymer melts," *J. Rheol.* **54**, 223–260 (2010).
- Waton, G., and R. Zana, "Relaxation in wormlike micelle solutions," in *Giant Micelles; Properties and Application*, Surfactant Science Series (CRC Taylor & Francis group, Boca Raton, 2007), Chap. 10.
- Willenbacher, N., C. Oelschlaeger, M. Schopferer, P. Fischer, F. Cardinaux, and F. Scheffold, "Broad bandwidth optical and mechanical rheometry of wormlike micelle solutions," *Phys. Rev. Lett.* **99**, 068302 (2007).
- Yamamoto, S., and S. Hyodo, "Mesoscopic simulation of the crossing dynamics at an entanglement point of surfactant threadlike micelles," *J. Chem. Phys.* **122**, 204907 (2005).
- Yusof, N. S. M., and M. N. Khan, "Quantitative correlation of counterion (X) affinity to ionic micelles and X- and temperature-induced micellar growth (spherical—wormlike micelles—vesicles) for X = 5-Methyl- and 5-Methoxysalicylate ions," *J. Phys. Chem. B* **116**, 2065–2074 (2012).
- Zdziennicka, A., K. Szymczyk, J. Krawczyk, and B. Jańczuk, "Critical micelle concentration of some surfactants and thermodynamic parameters of their micellization," *Fluid Phase Equilib.* **322–323**, 126–134 (2012).
- Zou, W., and R. G. Larson, "A mesoscopic simulation method for predicting the rheology of semi-dilute wormlike micellar solutions," *J. Rheol.* **53**, 681–721 (2014).